The PUMA project. III. Incidence and properties of ionised gas disks in ULIRGs, associated velocity dispersion and its dependence on starburstiness

M. Perna[1,2]⋆, S. Arribas[1], L. Colina[1], M. Pereira Santaella[1], I. Lamperti[1], E. Di Teodoro[3,4], H. Übler[5,6], L. Costantin[1,7], R. Maiolino[5,6,8], G. Cresci[2], E. Bellocchi[9], C. Catalán-Torrecilla[1], S. Cazzoli[10], and J. Piqueras López[1]

[1] Centro de Astrobiología, (CAB, CSIC–INTA), Departamento de Astrofísica, Cra. de Ajalvir Km. 4, 28850 – Torrejón de Ardoz, Madrid, Spain
[2] INAF - Osservatorio Astrofisico di Arcetri, Largo Enrico Fermi 5, I-50125 Firenze, Italy
[3] Department of Physics & Astronomy, Johns Hopkins University, Baltimore, MD 21218, USA
[4] Space Telescope Science Institute, 3700 San Martin Drive, Baltimore, MD 21218, USA
[5] University of Cambridge, Cavendish Laboratory, Cambridge CB3 0HE, UK
[6] University of Cambridge, Kavli Institute for Cosmology, Cambridge CB3 0HE, UK
[7] INAF - Astronomical Observatory of Brera, via Brera 28, I-20121 Milano, Italy
[8] Department of Physics and Astronomy, University College London, Gower Street, London WC1E 6BT, UK
[9] Centro de Astrobiología (CSIC-INTA), ESAC Campus, 28692 Villanueva de la Cañada, Madrid, Spain
[10] IAA - Instituto de Astrofísica de Andalucía (CSIC), Apdo. 3004, 18008, Granada, Spain

ABSTRACT

Context.

Aims. A classical scenario suggests that ULIRGs transform colliding spiral galaxies into a spheroid-dominated early-type galaxy. Recent high-resolution simulations have instead shown that, under some circumstances, rotation disks can be preserved during the merging process or rapidly regrown after coalescence. Our goal is to analyze in detail the ionised gas kinematics in a sample of ULIRGs to infer the incidence of gas rotational dynamics in late-stage interacting galaxies and merger remnants.

Methods. We analysed integral field spectrograph MUSE data of a sample of 20 nearby ($z < 0.165$) ULIRGs (with 29 individual nuclei), as part of the "Physics of ULIRGs with MUSE and ALMA" (PUMA) project. We used multi-Gaussian fitting techniques to identify gaseous disk motions, and the 3D-Barolo tool to model them.

Results. We found that 27% (8/29) individual nuclei are associated with kpc-scale disk-like gas motions. The rest of the sample displays a plethora of gas kinematics, dominated by winds and merger-induced flows, which make the detection of rotation signatures difficult. On the other hand, the incidence of stellar disk-like motions is $\lesssim 2$ times larger than gaseous disks, as the former are probably less affected by winds and streams. The eight galaxies with a gaseous disk present relatively high intrinsic gas velocity dispersion ($\sigma_0 \in [30 - 85]$ km s^{-1}), and rotationally-supported motions (with gas rotation velocity over velocity dispersion $v_{rot}/\sigma_0 \gtrsim 1 - 8$), and dynamical masses in the range $(2 - 7) \times 10^{10}$ M$_\odot$. By combining our results with those of local and high-z (up to $z \sim 2$) disk galaxies from the literature, we found a significant correlation between σ_0 and the offset from the main sequence (δMS), after correcting for their evolutionary trends.

Conclusions. Our results confirm the presence of kpc-scale rotating disks in interacting galaxies and merger remnants in the PUMA sample, with an incidence going from 27% (gas) to $\lesssim 50\%$ (stars). Their gas σ_0 is up to a factor of ~ 4 higher than in local normal MS galaxies, similar to high-z starbursts as presented in the literature; this suggests that interactions and mergers enhance the star formation rate while simultaneously increasing the velocity dispersion in the interstellar medium.

Key words. Galaxies:active - Galaxies: starburst - Galaxies: ISM - Galaxies: interactions - Galaxies: kinematics and dynamics

1. Introduction

Local ultraluminous infrared galaxies (ULIRGs, with rest-frame $[8 - 1000 \ \mu m]$ luminosity L_{IR} in excess of $10^{12} L_\odot$) are an important class of objects for understanding the formation and evolution of massive galaxies. A classic evolutionary scenario (Sanders et al. 1988; Springel et al. 2005) suggests that ULIRGs evolve into elliptical galaxies through a merger-induced dissipative collapse. In this scenario, the gas of colliding galaxies loses angular momentum and energy, falling into the coalescing centre of the system. Here it serves as fuel for the starburst (SB) and the growth of a supermassive black hole (BH), in a dust enshrouded environment. Then, the system evolves into an optically bright quasar once it either consumes or removes shells of gas and dust through powerful winds. Finally, the merger remnant becomes an elliptical galaxy.

Recent theoretical works have pointed out that dissipative mergers can also lead to the formation of new disk galaxies. Gas that is not efficiently forced to collapse and form new stars, nor expelled by SB and active galactic nuclei (AGN) winds, can be preserved in a disk, or re-form a new disk plane and start regrowing a stellar disk (Robertson et al. 2006; Robertson & Bullock 2008; Bullock, Stewart & Purcell 2009; Governato et al. 2009;

Hopkins et al. 2009, 2013). Hydrodynamical simulations show that cold flows from filamentary structures also play a major role in the buildup of disks in galaxies (Kereŝ et al. 2005; Dekel et al. 2009; Governato et al. 2009). The interaction between inflows and outflows, the amount of gas, as well as the mass ratio of the merging galaxies and their orbital parameters (e.g. Hopkins et al. 2009), all affect the probability of preserving (or reforming) a disk.

From an observational point of view, ordered disk-like kinematics are generally observed in merger systems, both at low-z (Bellocchi et al. 2013; Medling et al. 2014; Ueda et al. 2014; Barrera-Ballesteros et al. 2015; Perna et al. 2019) and at high-z (up to $z \gtrsim 4$; e.g. Hammer et al. 2009; Alaghband-Zadeh et al. 2012; Harrison et al. 2012; Perna et al. 2018; Leung et al. 2019; Tadaki et al. 2020; Cochrane et al. 2021).

Recently, we started a project aimed at studying, at sub-kpc scales, the 2D multi-phase outflow structure in a representative sample of 25 local ULIRGs, by comparing the capabilities offered by the ALMA interferometer and the VLT/MUSE integral field spectrograph. The project, labelled PUMA - Physics of ULIRGs with MUSE and ALMA - is described in the first paper of a series, Perna et al. (2021; Paper I hereinafter). First MUSE data results are also presented in Paper I: we derived stellar kinematics for all the PUMA systems, and found that post-coalescence systems are more likely associated with disk-like motions, while interacting (binary) systems are dominated by non-ordered and streaming motions. We also investigated the presence of nuclear outflows associated with the individual nuclei, and found ionised and neutral outflows in almost all individual nuclei of our ULIRGs sample. A more comprehensive study of physical and kinematic properties of the interstellar medium (ISM) of the archetypical ULIRG Arp 220 was instead presented in Perna et al. (2020, as part of the PUMA project). In Pereira-Santaella (2021; Paper II hereinafter) we instead analysed the $\sim$ 220 GHz and CO(2-1) ALMA observations to constrain the hidden energy source of ULIRGs, providing evidence for the ubiquitous presence of obscured AGN that could dominate their infrared emission.

The PUMA sample also allows us to investigate the presence of rotational motions in connection with inflows and outflows in dissipative mergers, and therefore to test the predictions of hydrodynamical simulations. Hence, the present paper is aimed at investigating the prevalence of gas rotational motions in the inner regions of PUMA systems, as well as their (mis)alignments with the stellar component. In this work, we also characterise the kinematic properties of the associated disk structures in terms of inclination, rotational velocity, velocity dispersion, and dynamical mass. Finally, we compare PUMA properties with those of other local (U)LIRGs and high-z populations of normal main sequence (MS) and SB galaxies, studying the variation of the gas velocity dispersion as a function of the star formation rate SFR and the starburstiness of the system, defined as the ratio between the specific SFR (sSFR = SFR/M$_*$) of a galaxy and the sSFR of a MS galaxy with the same z and M$_*$ ($\delta MS = sSFR/sSFR|_{MS}$; e.g. Elbaz et al. 2011).

This paper is organised as follows. In Sect. 2 we briefly summarise the PUMA sample selection, and present the data analysis of spectroscopic (MUSE) and photometric (HST) data. In Sects. 3.1-3.4 we report the main results obtained from the spectroscopic analysis, in terms of incidence of disk-like motions in the gas and stellar components, and also compare the gas and stellar motions along their kinematic major axes. For those systems with disk-like gas motions, in Sect. 3.5 we present 3D-Barolo modelling and infer a kinematic classification in terms of the ra-

tio between rotational velocity and intrinsic velocity dispersion. Sect. 3.6 presents the study of correlations between intrinsic velocity dispersion and SFR and starburstiness in an extended sample of MS and SB galaxies in the redshift range $z \sim 0.03 - 2.6$. Finally, Sect. 4 summarises our conclusions. Throughout this paper, we adopt the cosmological parameters $H_0 = 70$ km/s/Mpc, $\Omega_m = 0.3$, and $\Omega_\Lambda = 0.7$.

2. Methods

2.1. Sample

The PUMA sample is a volume-limited ($z < 0.165$; d < 800 Mpc) representative sample of 25 local ULIRGs. The sample selection is described in detail in Paper I. In brief, the targets were selected among the IRAS 1 Jy Survey (Kim & Sanders 1998), the IRAS Revised Bright Galaxy sample (Sanders et al. 2003), and the Duc et al. (1997) catalogue, isolating the sources visible by ALMA and MUSE and uniformly covering the ULIRG luminosity range. The sample was also selected to include an equal number of systems with AGN and SB nuclear activity (based on mid-IR spectroscopy) in the pre- and post-coalescence phases of major mergers (with projected nuclear distances lower than 10 kpc).

So far, we have obtained MUSE observations for 85% of the systems in the sample (21 systems with 31 individual nuclei; see Tables 1 and 2 in Paper I), and ALMA CO(2–1) and $\sim$ 220 GHz continuum observations for the entire sample (22 systems, with 32 individual nuclei, have been already presented in Paper II). In this work, we focus on the kinematic properties of the ionised gas of the 20 ULIRGs (with 29 individual nuclei) observed with MUSE, therefore excluding the Arp 220 system whose properties have been extensively described in Perna et al. (2020, but see also Appendix B for a brief description of its kinematics). Information about the MUSE data used in this work are collected in Paper I, Table 2. At the mean distance ($\sim$ 400 Mpc), the MUSE spaxel scale, resolution, and FoV correspond to $\sim$ 0.34 kpc (0.2″), $\sim$ 1 kpc (0.6″), and $\sim$ 100 × 100 kpc^2 (60″ × 60″).

2.2. Data analysis

In this section we describe the MUSE spectroscopic and HST imaging data analysis we followed to characterise the kinematics and dynamics in our PUMA targets.

2.2.1. MUSE spectroscopic analysis

The MUSE data reduction and analysis was executed by following an approach similar to that described in Paper I. We briefly summarise it in the following. The data reduction and exposure combination were carried out by using the ESO pipeline (muse - 2.6.2). The astrometric registration was performed using the Gaia DR2 catalogue (Gaia Collaboration 2018) for all but 5 systems, for which we used registered HST optical images as reference (because of the absence of Gaia stars in the MUSE field of view (FOV); see Paper I, section 3.1 for more details).

We first fitted and subtracted the stellar continuum from each spaxel. To do so, we initially performed a Voronoi binning (Cappellari & Copin 2003) on the cube to achieve a minimum signal-to-noise ratio (S/N > 16) per bin on the continuum. We then fitted the stellar continuum in each bin through the pPXF code (Penalized PiXel-Fitting; Cappellari & Emsellem 2004; Cappellari 2017), using the Indo-U.S. Coudé Feed Spectral Library (Valdes et al. 2004) as stellar spectral templates to model the
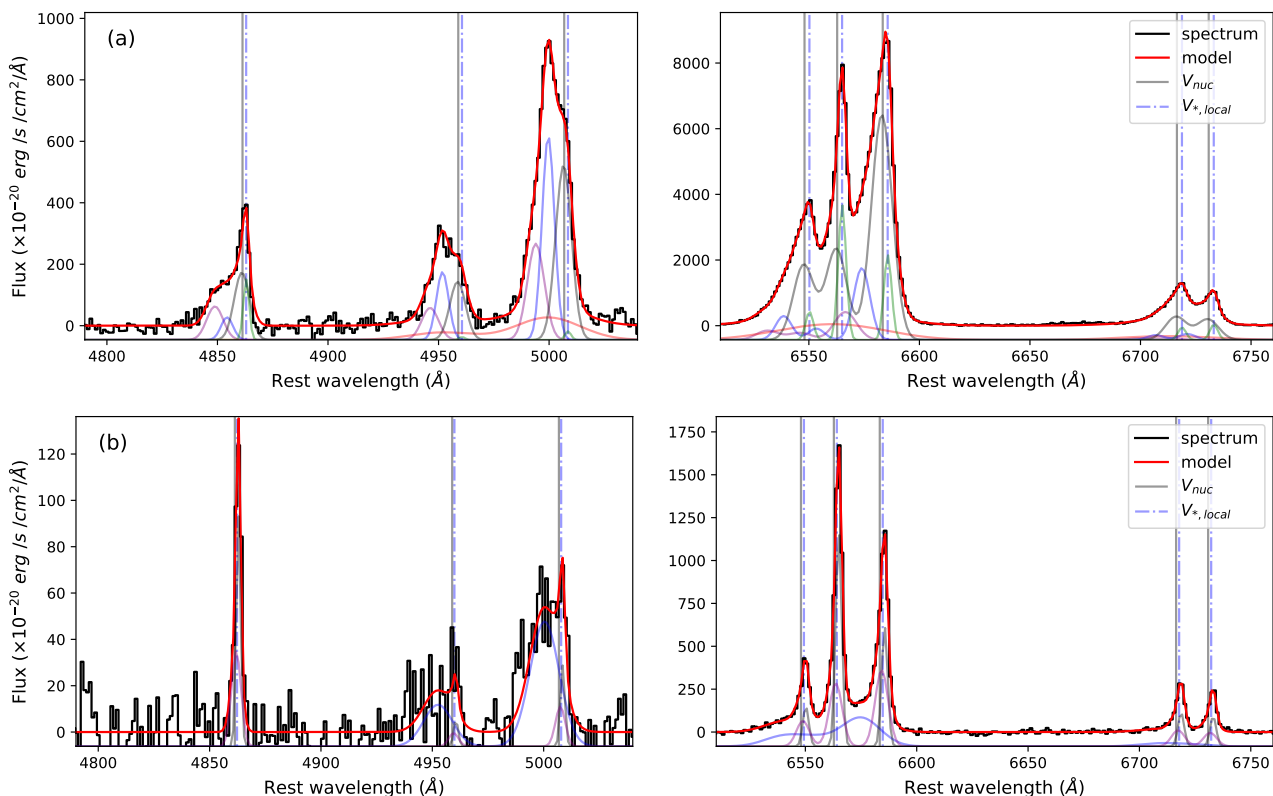
Fig. 1: Examples of our multi-component Gaussian fit decomposition for two continuum-subtracted spectra of I13120, extracted from single spaxels at ~ 1″ (top panels) and 2″ (bottom) south-east from the nucleus. The red curves show the best-fit solutions in the Hβ-[OIII] (left) and Hα-[NII] (right) regions; all emission lines are fitted simultaneously. The solid vertical lines mark the rest frame wavelength of the emission lines, derived from the stellar velocities of the nuclear spectrum; the dot-dashed blue vertical lines mark instead the local stellar systemic (i.e. at the position of the spaxel from which the spectrum is extracted). These examples demonstrate the diversity of emission-line profiles observed in the FOV of a single target: the spectrum in panels (*a*) is dominated by broad and blueshifted Gaussian components, while the one in panel (*b*) is dominated by bright narrow Gaussians close to the systemic velocity (for all but [OIII] lines).

stellar continuum emission and absorption line systems. We then subtracted the stellar continuum from the total spectra in each spaxel, scaling the fit from bin to each spaxel according to the observed continuum flux (see Paper I, sect. 5.1).

A slightly different approach was instead used for the two Seyfert 1 in our sample, IZw1 and I01572: in addition to the stellar spectral templates, we made use of an AGN template constructed on the basis of the observed nuclear spectrum, modelled with a combination of a power-law continuum, forbidden, and permitted emission lines as described in Paper I, Appendix B. Because of the point-spread-function blending, this AGN component accounts for a significant fraction of the total emission in the innermost nuclear regions, and rapidly reduces going to radii $r \gtrsim 1''$. This step allows us to better reconstruct the stellar velocity field in the nuclear regions with respect to our previous analysis results (see Fig. 5 in Paper I, and Fig. C.1, top-right in this work).

Before proceeding with the fit of the emission lines, we derived a second Voronoi tessellation to achieve a minimum S/N = 8 of the Hα line for each bin. This feature has been preferred to the [OIII]λ5007 line, generally used to trace ionised outflows, as the latter is highly absorbed in ULIRG systems due to their large dust content. The use of Hα as a reference for the tessellation allows us to better preserve the important spatial information (both for kinematics and emission line structures).

At this point we fitted the most prominent gas emission lines from the continuum-subtracted cube, by using the Leven-

berg–Markwardt least-squares fitting code CAP-MPFIT (Cappellari 2017). In particular, we modelled the Hβ and Hα lines, the [O III]$\lambda\lambda$4959,5007, [N II]$\lambda\lambda$6548,83, [S II]$\lambda\lambda$6716,31, and [O I]$\lambda\lambda$6300,64 doublets with a simultaneous fitting procedure. To account for broad and asymmetric line profiles, already observed in the nuclear regions of almost all PUMA targets (Paper I), we performed each spectral fit five times at maximum, with one to five kinematic components (i.e. Gaussian sets, each centred at a given velocity and with a given FWHM). The final number of kinematic components used to model the spectra was derived on the basis of the Bayesian information criterion (BIC, Schwarz 1978). A detailed description of the Gaussian fit routine can be found in Paper I and Perna et al. (2020).

In Fig. 1 we show two examples of our continuum-subtracted, high S/N spectra, extracted from two different regions of the target 13120−5453 (I13120 hereafter). The best-fit models show the presence of broad and asymmetric line profiles in the two spectra, and a significant diversity in the relative contribution of narrow and broad components: the emission lines in the spectrum in the (*a*) panels are dominated by the contribution of extremely broad Gaussian components, while the ones in the (*b*) panels have a well defined narrow core, especially in the Balmer transitions, associated with less perturbed gas. These two examples show that a multi-component simultaneous fit of all prominent optical emission lines is required to properly separate ordered and perturbed motions in our PUMA systems.

Table 1: PUMA geometric properties and stellar and narrow Hα velocities along the kinematic major axis

IRAS ID (other)	$2R_e$ (kpc)	i^{morph} (deg)	PA^{morph} (deg)	PA_*^{kin} (deg)	PA_{gas}^{kin} (deg)	δv_* (km s^{-1})	δv_{gas} (km s^{-1})	$\bar{\sigma}_*$ (km s^{-1})	$\bar{\sigma}_{gas}$ (km s^{-1})	disk-like kin
(1)	(2)	(3)	(4)	(5)	(6)	(7)	(8)	(9)	(10)	(11)
F00188−0856	1.5 ± 0.1	26 ± 12^s	5 ± 1^u	93 ± 9	81 ± 16	145 ± 7	77 ± 2	23^{+8}_{-15}	107^{+2}_{-5}	s
F00509+1225 (IZw1)	3.68 ± 0.05	36 ± 14^s	23 ± 2^u	130 ± 3	130 ± 3	270 ± 2	370 ± 10	3 ± 2	57^{+11}_{-18}	s, g
F01572+0009	3.81 ± 0.05	37 ± 14^s	33 ± 2^u	68 ± 3	−	178 ± 17	300 ± 10	100^{+2}_{-12}	140^{+11}_{-17}	s
F05189−2524	0.5 ± 0.1	34 ± 14^s	39 ± 4^u	68 ± 3	−	125 ± 3	125 ± 6	10 ± 2	100 ± 2	s
F07251−0248 E	−	−	−	−	−19 ± 3	95 ± 9	170 ± 10	95^{+4}_{-7}	114 ± 1	−
F07251−0248 W	−	−	−	112 ± 3	106 ± 3	197 ± 7	325 ± 10	69^{+2}_{-4}	103^{+3}_{-6}	s?, g?
F09022−3615	−	−	−	25 ± 3	−	290 ± 4	190 ± 6	120^{+2}_{-5}	125^{+6}_{-10}	−
F10190+1322 E	−	−	−	68 ± 3	93 ± 3	278 ± 28	265 ± 8	85 ± 2	118^{+2}_{-8}	s, g
F10190+1322 W	5.2 ± 0.3**	46 ± 15^s	131 ± 5^s	118 ± 3	106 ± 3	244 ± 3	310 ± 2	7^{+2}_{-5}	63 ± 2	s, g
F11095−0238 NE	−	−	−	−	−	−	−	−	−	−
F11095−0238 SW	−	−	−	−	−	−	−	−	−	−
F12072−0444 N	−	−	−	99 ± 12	74 ± 6	188 ± 2	130 ± 2	17 ± 14	107^{+4}_{-14}	s, g
F12072−0444 S	−	−	−	−	−	−	−	−	−	−
13120−5453	1.1 ± 0.1	25 ± 11^s	102 ± 2^u	99 ± 3	93 ± 3	214 ± 3	328 ± 2	98^{+6}_{-18}	78^{+1}_{-5}	s, g
F13451+1232 E	−	−	−	−	−	−	−	−	−	−
F13451+1232 W	−	−	−	−	−	−	−	−	−	−
F14348−1447 NE	−	−	−	19 ± 3	174 ± 3	154 ± 8	180 ± 7	90 ± 2	90 ± 2	s?, g?
F14348−1447 SW	−	−	−	174 ± 3	−	181 ± 4	47 ± 5	84 ± 2	101 ± 2	s
F14378−3651	1.4 ± 0.1	25 ± 11^s	29 ± 3^u	12 ± 3	25 ± 9	129 ± 5	84 ± 3	49 ± 14	85^{+1}_{-6}	s
F16090−0139	9.4 ± 0.5**	38 ± 15^s	11 ± 2^s	145 ± 3	168 ± 3	145 ± 16	182 ± 3	150^{+7}_{-15}	120^{+3}_{-7}	s?
F17208−0014	2.4 ± 0.1**	40 ± 15^s	173 ± 3^s	155 ± 4	155 ± 3	206 ± 10	210 ± 4	177 ± 3	126 ± 2	s?, g?
F19297−0406 S	−	−	−	59 ± 3	−	217 ± 12	270 ± 5	134^{+4}_{-15}	126 ± 7	−
F19297−0406 N	−	−	−	62 ± 3	−	160 ± 3	160 ± 13	141 ± 4	130^{+5}_{-9}	−
19542+1110	1.1 ± 0.1	16 ± 9^s	58 ± 3^s	56 ± 3	−	182 ± 2	97 ± 7	5 ± 2	122^{+2}_{-9}	s
20087−0308	2.8 ± 0.1**	36 ± 14^s	82 ± 2^s	87 ± 6	50 ± 3	137 ± 8	353 ± 6	146^{+7}_{-22}	116 ± 4	s?, g?
20100−4156 NW	−	−	−	−	−	−	−	−	−	−
20100−4156 SE	3.0 ± 0.1**	56 ± 16^s	74 ± 1^s	74 ± 6	19 ± 3	154 ± 7	100 ± 6	12 ± 1	104 ± 2	s, g
F22491−1808 E	−	−	−	−	155 ± 6	56 ± 2	77 ± 5	81 ± 5	105 ± 2	−
F22491−1808 W	−	−	−	−	−	−	−	−	−	−

Notes.
Column (1): target name. Column (2): $2R_e$ from *Isophote* fits of available HST/F160W images for all but the Seyfert 1 systems IZw1 and I01572 (for which we used the Veilleux et al. 2006 measurements) and the two systems without HST data: I16090 and I10190. The geometric parameters of the latter two sources are derived from MUSE narrow-band images (at $\lambda \sim 7500$Å). Columns (3) and (4): inclination and PA of the galaxy. The PA is taken anticlockwise from the North direction on the sky. These parameters are derived with *Isophote*, at the distance reported in Column (2). Columns (5) and (6): stellar and gas PA^{kin}, taken anticlockwise from the North direction on the sky. Column (7) and (8): maximum stellar and gas velocity variations along PA^{kin}, non-corrected for galaxy inclination. The velocity amplitudes are computed along an intermediate PA^{kin} when PA_*^{kin} and PA_{gas}^{kin} are consistent within the errors (3σ); alternatively, stellar (gas) velocity amplitudes are computed along PA_*^{kin} (PA_{gas}^{kin}); for those sources with a missing PA^{kin} measurement, the gas and stellar δv are computed along the only available PA^{kin} measurement. Velocity uncertainties are derived with a bootstrap. Columns (9) and (10): median velocity dispersion along PA^{kin}. All velocity and velocity dispersion values for the gas component are derived from the narrow Hα velocity maps. Column (11): kinematic classification according to the two criteria defined in Sect. 3.2: 's' for stellar disk-like kinematics; 'g' for gas disk-like kinematics.
(**): The effective radius measurement is highly uncertain, due to prominent tidal tails (and, for I10190 W, the nearby E nucleus).
(^{s}): in Columns 3 and 4, the label identifies those sources which geometric parameters do not vary significantly at $r > R_e$, i.e. which inclination and PA are relatively stable.
(^{u}): in Columns 3 and 4, the label identifies those sources which inclination and PA vary significantly at $r > R_e$. These sources generally have prominent tails which strongly affect the *isophote* fit.

2.2.2. Complementary photometric analysis

We made use of the Photutils (Bradley et al. 2016) *Isophote* package of Astropy (Astropy Collaboration 2018) to perform a basic photometric analysis of ancillary HST near-infrared images, available for most of our targets. This analysis provides important morphological parameters to be compared with those inferred from the kinematic analysis described in the next sections.

We fitted a series of isophotal ellipses to each galaxy: *Isophote* was instructed to hold the centre position constant, whereas the ellipticity (ϵ) and position angle (PA) of the ellipses interpolating the galaxy isophotes were allowed to vary (e.g. Costantin et al. 2017, 2018). *Isophote* provides the azimuthally averaged surface brightness profile as well as the variation of ϵ and PA as a function of the semi-major axis length. In Table 1 we report the inferred inclinations, derived from ϵ following Willick et al. (1997), and PA at the galactocentric distance of two times the effective radius R_e, defined as the radius which contains half of the galaxy light (and computed adopting the curve-of-growth method; see e.g. Crespo Gómez et al. 2021). Morphological parameters are reported for a small fraction of sources (12/29 individual galaxies), as the intrinsic values of PUMA galaxies are usually distorted by merger interactions, and the presence of companion systems. These distortions are also sometimes responsible of significant variations in the morphological parameters at large radii ($r > R_e$); we therefore report

in the table whether the morphological inclination and PA do show significant variations at large distances.

Our rough estimates for R_e are in general agreement with those obtained in previous works, by a factor of 2 (Veilleux et al. 2006; Haan et al. 2011; Kim et al. 2013), for all but the two Seyfert 1 in our sample, IZw1 and I01572. For these two sources we therefore considered the distance obtained by Veilleux et al. (2006), who performed a more rigorous multi-component two-dimensional image decomposition to separate the host galaxy from its bright active nucleus.

In Sect. 3.4 we will compare the morphological PAs we derived with *Isophote* with the kinematic ones derived from MUSE spectroscopic analysis. The inclination measurements will be instead used to model the gas kinematics with 3D-Barolo (Di Teodoro & Fraternali 2015) in Sect. 3.5.

2.3. Emission line tracers and velocity parameters

Throughout this paper, we differentiate between the individual kinematic component parameters, FWHM_j and ΔV_j, with j from 1 to 5 at maximum, and the non-parametric velocities $v10$, $v50$, $v90$ and $W80$ (e.g. Liu et al. 2013). The former identify the width of a specific kinematic component, j, and its velocity shift with respect to the systemic, defined as the stellar velocity in the nuclear position (see Sect. 5.2 in Paper I); FWHM_j and ΔV_j are common to all emission lines fitted simultaneously. Instead, the non-parametric velocities are defined as follows: $v10$, $v50$ and $v90$ are the 10th, 50th, and 90th-percentile velocities, respectively, calculated on the (multi-component) fitted line profile with respect to the systemic. Therefore, they correspond to the velocities at which 10, 50 and 90% of the line flux is accumulated. $W80$ is defined as $v90 - v10$.

Observations of relatively large samples of AGN and star-forming galaxies (SFGs) have indicated that the Hα emission is not necessarily dominated by outflows as is the case for [OIII] emission lines (e.g. Bae & Woo al. 2014; Cicone et al. 2016), as the Balmer line has a significant contribution from star-forming regions. Indeed, the spectral analysis of the line emission coming from the nuclear regions of our PUMA systems already revealed that $v10$ and $W80$ of Hα are, on average, 20% smaller than those of the [OIII] (Paper I). Similarly, [NII] lines have a larger velocity-width than Hα, consistent with those of the [OIII] ($\langle W80$ [O III] / $W80$ [NII] $\rangle \sim \langle v10$ [O III] / $v10$ [NII] $\rangle = 1.05$). This empirical evidence can be explained taking into account the fact that [NII] is brighter than Hα both in AGN ionisation cones, often affected by gas flows (e.g. Fischer et al. 2013), and in shocks (e.g. Allen et al. 2008). Therefore, the nitrogen line may be better analogous to the [O III] emission, as preferentially traces outflows and more unsettled material compared to Hα (see also e.g. Harrison et al. 2016). Because of the high extinction in PUMA systems, [NII] has to be preferred to the (fainter) [OIII] as outflow tracer (see also Perna et al. 2020).

For each PUMA target, we produced emission line maps for the flux, $v50$, and $W80$ non-parametric velocities, obtained considering the total modelled line profiles made up of the sum of the fitted Gaussians. The Hα and [NII] maps of I13120 are presented in Fig. 2. These maps mark the dissimilarities mentioned above: the Hα velocity field appears more regular than the [NII] one; indeed the Hα map shows slightly smaller velocity-widths. The Hα and, in particular, the [NII] velocity maps show a biconical outflow structure, the approaching part to the south and the receding part to the north. Precisely, the $v50$ map shows high-v [NII] gas blueshifted to the south, within a conical region with a large opening angle, and high-v redshifted [NII] extending to

the north. The outflow biconical structure is also associated with high $W80$ (up to ~ 1000 km s^{-1}). We therefore conclude that, with respect to [NII] lines, Hα is less affected by outflows and highly perturbed kinematics.

In this paper we focus on the disentangling of ionised gas rotation dynamics in the PUMA sample; we therefore present all Hα maps in Appendix A, and leave the [NII] maps to a following investigation.

3. Results and discussion

3.1. Ionised gas kinematic decomposition

The velocity field of I13120 (Fig. 2) shows a regular velocity gradient along the east-west direction, in addition to the typical features observed in biconical outflows, like blue- and red-shifted emitting gas with increased line widths in regions preferentially located along the perpendicular direction. In order to understand if this system is rotationally supported, we take advantage of the kinematic decomposition described in Sect. 2.2. Figure 3, left, shows the distribution of ΔV_j and FWHM_j for each Gaussian component j used to model the emission line profiles in I13120. The figure shows a clear trend: highest FWHM_j ($\gtrsim 700$ km s^{-1}) are associated with significant blueshifts ($\Delta V_j \lesssim -400$ km s^{-1}), while Gaussian components with smaller FWHM_j have $|\Delta V_j| \lesssim 200$ km s^{-1}. The highest velocity shifts and line widths are associated with the outflow (see also e.g. Woo et al. 2016 for similar diagrams obtained from SDSS integrated spectra of nearby AGN); instead, the smallest velocities are associated with less perturbed kinematics. To better investigate the presence of rotationally supported motions, we select in the $\Delta V_j -$ FWHM_j plane the components with $|\Delta V_j| < 250$ km s^{-1} and $\text{FWHM}_j < 400$ km s^{-1} (see e.g. Mingozzi et al. 2019 for a similar approach), and construct a new data cube for the Hα emission, labelled narrow Hα data cube. The line width threshold $\text{FWHM}_j = 400$ km s^{-1} was chosen taking into account the fact that in our targets the stellar component, more sensitive to gravitational motions, has a velocity dispersion significantly smaller (with σ_* up to 200 km s^{-1} only in the innermost nuclear regions, due to beam smearing effects). The flux distribution as well as the velocity field and velocity dispersion of narrow Hα are reported in Fig. 3. As expected, the narrow Hα maps display more regular velocity patterns (and significantly lower line widths) with respect to those obtained from the total Hα (and [NII]) lines in Fig. 2.

In the next section, we investigate the presence of rotation in our PUMA systems, taking advantage of this kinematic decomposition between more and less perturbed Gaussian components in the $\Delta V_j -$$\text{FWHM}_j$ plane, and extracting for each target the position-velocity (PV) diagrams along the kinematic major axis of narrow Hα data cubes.

3.2. Kinematics along the major axis

Figure 4 shows the PV plots along the kinematic major axis position angle (PA^{kin}) of I13120, for both the total Hα emission (first panel) and the narrow Hα (second panel). A clear velocity gradient from ~ 200 km s^{-1} to ~ -200 km s^{-1} is observed in both panels; therefore, the exclusion of very-high velocity components does not introduce or alter significantly this gradient. In the same figure, we report the extracted line velocity centroids and velocity dispersion of the narrow Hα, as well as the stellar velocities (obtained from pPXF analysis, see Paper I) along the stellar component major axis. At this stage, no correction for the beam
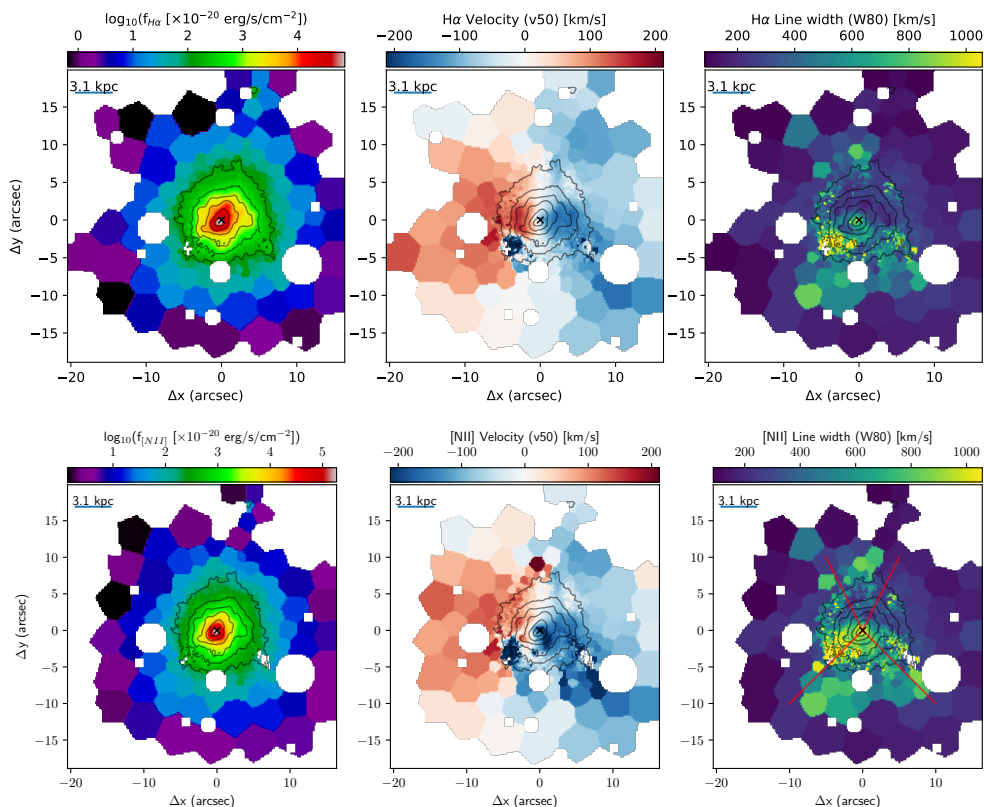
Fig. 2: I13120 maps. Top: total Hα integrated flux (left), Hα centroid (*v*50, centre) and line-width (*W*80, right) obtained from the multi-component Gaussian fit. Bottom: Similar panels for [NII]; in the *W*80 map, the red lines indicate the wide biconical outflow along the north-south direction. Masked regions mark the spaxels contaminated by the presence of background and foreground sources, and excluded as disturbing the data analysis. The first solid contour is 3σ and the jump is 0.5 dex. The cross marks the nucleus. North is up and West is right.
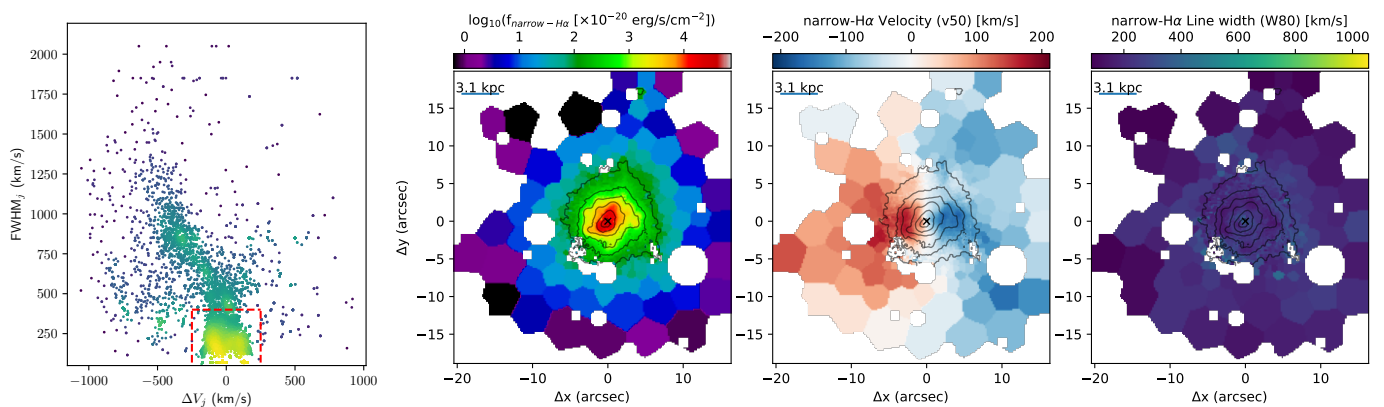
Fig. 3: *Left panel*: I13120 velocity shift ΔV_j-FWHM$_j$ diagram (colored by density in log-scale) for the individual Gaussian components used to model the emission line profiles in the data cube. The red dashed lines isolate the Gaussian components used to reconstruct the narrow Hα data cube, with $|\Delta V_j| < 250$ km s^{-1} and FWHM$_j < 400$ km s^{-1}. *Right panels*: the narrow Hα flux distribution, velocity (*v*50) and line width (*W*80) maps are reported in the 2nd, 3rd and 4th panels respectively (see Fig. 2 for details).

smearing is performed in the reported velocity dispersion. Both the narrow Hα and stellar components exhibit i) a well defined velocity gradient along their major axes, and ii) a peak in the velocity dispersion diagram at the position of the nucleus. These two conditions provide initial evidence for a rotation-dominated system (e.g. Förster Schreiber et al. 2018).

In Fig. B.1 we show the comparison between the narrow Hα and stellar velocities along their kinematic major axis, for the 18 targets for which we can observe a clear velocity gradient (and measure a PA^{kin}) together with a peak in the velocity

dispersion diagram at the position of the nucleus for at least one component (i.e. gas or stars). The PA^{kin} measurements, obtained with the python PaFit package (Krajnovic et al. 2006), the velocity amplitudes and median velocity dispersion measured along PA^{kin} are reported in Table 1 (columns 5 to 10), for both stellar and gas components.

The simple visual comparison between gas and stellar kinematics along PA^{kin} allows us to isolate 5 nuclei reasonably associated with more regular, disk-like kinematics for both gas and stellar components, according to the two criteria highlighted be-
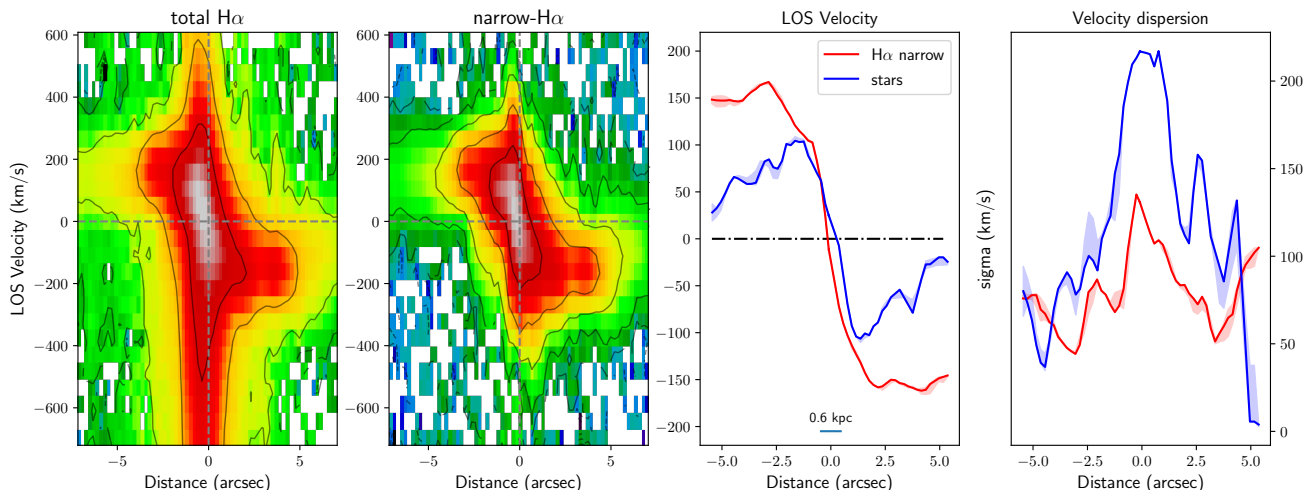
I13120 - major axis (PA = 93°)

Fig. 4: I13120 position-velocity diagrams along the galaxy major axis. *From left to right:* PV maps of the total Hα and the narrow Hα emission; the last two panels show the extracted line velocity centroids and line width of the narrow Hα, as well as the stellar velocities along the same axis. 1″ corresponds to ∼ 0.6 kpc at the distance of I13120, as labeled in the third panel.

fore: IZw1, I10190 W[1], I12072 N, I13120, I20100 S. The relatively small number of systems with such characteristics is due to the fact that PUMA consists of advanced interacting ULIRGs systems[2] with nuclear projected separations smaller than 10 kpc (i.e. systems classified as IIIb, IV, and V in the Veilleux et al. 2002 scheme). The small number of sources (5) with stellar and gas disk-like kinematics does not allow us to infer any specific conclusion about the conditions possibly related to more regular motions, also because of the different intrinsic properties of these systems: IZw1 has a small companion at ∼ 18 kpc; I10190 and I20100 have two nuclei separated by ≳ 5 kpc, and prominent tidal features; I12072 has two nuclei at a projected distance of ∼ 2.3 kpc; I13120 has a single nucleus and extended tails and loops surrounding the main body of the galaxy (up to ≳ 20 kpc from the nucleus; see e.g. Fig. 1 in Privon et al. 2016).

The rest of the sample displays a variety of kinematics. In the last column of Table 1 we distinguish among systems with evidence for disk-like kinematics in gas and stellar components. For instance, I07251 W, I14348 NE and I17208 do not have well defined kinematic properties: they might present disk-like motions, but with kinematic centres possibly not coincident with the nuclear position (see Fig. B.1). We note however that these small offsets might also be due to different amount of dust or the presence of tidal streams along the major axis PA (see e.g. Hα flux distribution in Fig. A.14). A better investigation of these offsets is reported in Appendix C. I20087 has peculiar outflow features, reasonably responsible of the observed velocity gradient (with a maximum variation δv_{gas} ∼ 353 km/s, a factor 2.6 higher than δv_*). Finally, there are 7 systems with regular stellar kinematics but highly perturbed gas motions, with σ_{gas} generally higher than 100 km/s across the major axis, and without clear trends in the LOS velocity: I00188, I01572, I05189, I14348 SW, I14378 and I19542 (with the possible addition of I16090, affected by poor data quality). A more detailed description of individual targets is reported in Appendix B.

Summarising, we found five systems with regular, disk-like kinematics traced by the narrow Hα and stars on scales of ≳ 6 kpc (in diameter), IZw1, I10190 W, I12072 N, I13120 and I20100 S, with the possible inclusion of three additional targets (I14348 NE, I17208 and I07251). The remaining targets (21/29 individual nuclei) show more complex gas kinematics, dominated by tidal streams (e.g. I09022 in Fig. A.6), loops (e.g. I05189 in Fig. A.4) and outflows (e.g. I13451 in Fig. A.10) that prevent a clear identification of possible features due to more regular, disk-like motions. On the other hand, the incidence of stellar disk-like motions is slightly higher than rotating gas, with 13 (17, including the more uncertain systems in Table 1) systems out of 29. This higher incidence is probably due to the fact that the stellar component is less affected by non-gravitational perturbations (shocks, outflows). Therefore, the incidence of gas disk-like kinematics in our PUMA sample, of 27% (8/29), has to be considered as lower limit. In support of this perspective, we note that in a merger, the gas has shorter dissipative timescales than stars, thus it should settle back on a rotating disk earlier than stars (e.g. Springel & Hernquist 2005).

Rodriguez-Gomez et al. (2017) analysed the morphology of ∼ 18000 central galaxies at z ∼ 0 from the Illustris cosmological hydrodynamic simulation (Sijacki et al. 2015). They found that, for objects with $M_* \lesssim 10^{11}$ M$_\odot$, mergers do not seem to play any significant role in determining the galaxy morphology: remnants are associated with both spheroidal and disk-dominated galaxies (see also Sparre & Springel 2014 for similar results). An incidence of ∼ 27 − 50% for rotating disks in our PUMA sample is therefore consistent with these theoretical predictions.

We stress however that the PUMA sample, with its relatively small number of targets and the different intrinsic properties of each ULIRG, limits the statistical meaning of our results. Among the 8/29 systems with gaseous disk-like kinematics, I10190 W, I14348 N and I20100 SE are associated with less advanced stages of the merger (wide binaries with nuclear separations ≳ 5 kpc in projection), and we cannot exclude a disk destruction in subsequent phases; IZw1 is instead a minor merger. On the other hand, the four remaining targets have a unique kinematic centre and kpc-scale rotation signatures, regardless the presence of double nuclei (in the binary systems I07251 and I12072) or

---

[1] We exclude I10190 E, as its gas kinematics in the receding part are dominated by those of the W nucleus.

[2] With the exception of IZw1, a minor merger system with log $L_{IR}/L_\odot$ = 11.3 but log $L_{bol}/L_\odot$ > 12.

strong streams (in the remnants I13120 and I17208). Among the other systems, we identified 5 merger remnants with a stellar disk (I00188, I01572, I05189, I14378 and I19542) but highly perturbed gas kinematics which might prevent the detection of a gaseous disk. These 9 targets (4 with a gaseous disk and 5 with a stellar disk) represent the strongest evidence for the preserving (or reforming) of a gaseous disk in major merger processes within the PUMA sample.

3.3. Differences between gas and stellar kinematics along major axis PA^{kin}

The narrow Hα and stellar PV diagrams in Fig. 4 (3rd and 4th panel) display significant dissimilarities: the maximum gas and stellar velocity variations along PA^{kin} are $\delta v_{gas} \sim 328$ km s^{-1}and $\delta v_* \sim 214$ km s^{-1}respectively, while the peak velocity dispersion are $\sigma_{gas} \sim 140$ km s^{-1}and $\sigma_* \sim 210$ km s^{-1}. Differences between gas and stellar kinematics along PA^{kin} are usually observed in (U)LIRGs (e.g. Cazzoli et al. 2014; Crespo Gómez et al. 2021), and can be interpreted as due to the presence of different dynamical structures or distinct levels of obscuration (see below).

A precise comparison between stellar and gas rotation along PA^{kin} can be performed only for a couple of systems in our sample. Among the 8 systems isolated in the previous section (IZw1, I07251 W, I10190 W, I12072 N, I13120, I14348 NE, I17208, and I20100 S), only two targets show regular gas PV diagrams, without significant contributions from perturbed components: I10190 W and I13120[3]. These two systems show similar maximum stellar and gas velocities, with $\delta v_{gas} \sim 200$ km s^{-1}and $\delta v_* \sim 300$ km s^{-1}, and similar maximum gas velocity dispersion, of ~ 130 km s^{-1}; vice versa, their maximum stellar velocity dispersion are significantly different, with $\sigma_* \sim 200$ km s^{-1}in I13120 and ~ 80 km s^{-1}in I10190 W. This difference might be due to intrinsic dissimilarities, as for instance the nuclear obscuration. As dust preferentially obscures young stars, which tend to be dynamically cooler than older stellar populations, an higher obscuration in the nuclear regions could translate into a higher velocity dispersion. The continuum color of I13120, defined as log (f_R/f_B), with f_R and f_B being the flux at ~ 9000Å and ~ 4500Å respectively, is a factor ~ 3 higher than I10190 W in the nuclear regions (Paper I). The different R_e of the two systems (see Table 1) could play a role as well: at fixed disk mass, a more compact disk has a steeper inner velocity gradient, resulting into a higher velocity dispersion peak.

Instead, the observed differences between stellar and gas velocity amplitudes in I10190 W and I13120 ($\delta v_{gas} \sim 1.5\delta v_*$) can be related to the star formation activity during the merger stages. For instance, numerical simulations by Cox et al. (2006) showed that old stars that are present prior to the merger, i.e. the oldest stellar populations, are the slowest rotators in a merger remnant; on the contrary, younger stars forming during the first passage of the galaxies and the final merger event are the fastest rotators (see their Fig. 7). We might speculate that youngest stars do not significantly contribute to the measured stellar velocity dispersion, as they are more embedded in dusty regions. In Catalán-Torrecilla et al. (in prep.) we will present the stellar population synthesis and its spatial distribution, in order to test this scenario.

---

[3] IZw1 PV diagrams are strongly affected by the AGN in the vicinity of the nucleus; similarly, the gas velocity profiles of remaining systems are affected by residual outflow and stream components; see Appendix B.
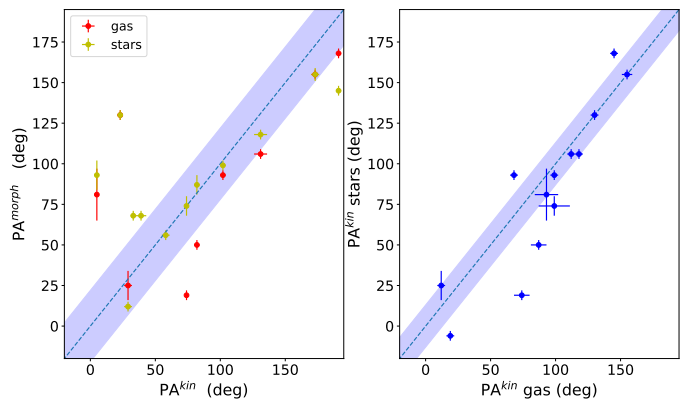
Fig. 5: *Left*: comparison between morphological and kinematic major axis PA for the stellar (yellow) and gas (red) components. The blue dashed line indicates the 1:1 relation; the blue shaded region ($\pm 22°$) includes 90% of the morpho-kinematic PA misalignments of a sample of 80 non-interacting galaxies from the CALIFA survey (Barrera-Ballesteros et al. 2015). *Right*: comparison between stellar and gas kinematic major axis PAs. The dashed line indicates the 1:1 relation; the shaded region ($\pm 15°$) includes 90% of the kinematic PA misalignments of CALIFA non-interacting galaxies (Barrera-Ballesteros et al. 2015).

3.4. Morpho-kinematic PA (mis)alignments

Figure 5, left, shows the comparison between morphological and (gas and stellar) kinematic major axis position angles, for all PUMA systems where it was possible to determine PA^{kin}. Following Barrera-Ballesteros et al. (2015), we compare our morpho-kinematic (mis)alignments with those of a control sample of 80 non-interacting galaxies from the CALIFA survey, whose spatial sampling (from ~ 0.3 to 1.5 kpc) and FOV coverage (sizes from 7 to 40 kpc) are comparable with those of our PUMA galaxies. In the figure, we report the 1:1 relation, with a shaded region including 90% of the CALIFA non-interacting sources, i.e. with a misalignment smaller than 22°. The relatively small PUMA sample does not allow us to derive strong conclusions about the general behaviour of ULIRGs systems; nevertheless, we note that 57% (4/7) of PUMA systems have $|PA^{morph} - PA^{kin}_{gas}|$ misalignments larger than 22°, and 42% (5/12) have $|PA^{morph} - PA^{kin}_*| > 22°$. These results are consistent with those reported by Barrera-Ballesteros et al. (2015), who analysed the morpho-kinematic misalignments in a larger sample of ~ 80 interacting CALIFA galaxies, considering both stellar and gas kinematic PAs.

Figure 5, right, shows instead the comparison between gas and stellar kinematic position angles, for the 13 PUMA systems where it was possible to determine the major axis PAs. Also in this case, we compare our results with those in Barrera-Ballesteros et al. (2015): in the figure, we report the 1:1 relation, with a shaded region including 90% of the CALIFA non-interacting sources, i.e. with a misalignment smaller than 15°. About 38% (5/13) PUMA kinematic misalignments are larger than 15°, roughly consistent with Barrera-Ballesteros et al. (2015), who find that 20% of the CALIFA interacting sample has kinematic misalignments larger than 15°.

The most deviating points in Fig. 5, right, are associated with I10190 E, I14348 NE, I16090, I20087, I20100 SE (see Table 1). The slightly larger number of PUMA systems with more extreme kinematic misalignments might be due to their more advanced merger stage with respect to CALIFA interacting galaxies, which sample contains $\gtrsim 43\%$ pre-merger systems without

any visual feature of interaction and projected distances up to 160 kpc. In fact, the presence of more close companions, prominent tidal streams, and strong nuclear winds in our PUMA systems might all contribute to the kinematic misalignments (but see also Chen et al. 2016).

These results indicate that interactions and mergers do have an impact on the internal kinematic alignment of galaxies. However, we note that stellar and gas PAs are roughly aligned, while more significant misalignments can be found between the morphological and kinematic PAs, consistent with the Barrera-Ballesteros et al. (2015) results.

3.5. 3D-Barolo and gas kinematics classification

To test whether the systems with more regular gas kinematics are compatible with a rotationally supported system, we modelled the narrow Hα data cubes with 3D-Barolo (Di Teodoro & Fraternali 2015). In particular, we modelled the gas kinematics of the following systems: IZw1, I07251, I10190 W, I12072 N, I13120, I14348 NE, I17208 and I20100 SE. In this section, we present the general strategy adopted for I13120; more details about the fitting procedure per individual targets are reported in Appendix C.

The main assumption of the 3D-Barolo model is that all the emitting material of the galaxy is confined to a geometrically thin disk and its kinematics are dominated by pure rotational motion. The possible presence of residual components associated with the outflow might affect the 3D-Barolo modelling, especially in the innermost nuclear regions, where the outflow is stronger. Nevertheless, this model allows us to asses the presence of such disks, and to infer a simple kinematic classification through the standard v_{rot}/σ_0 ratio, where v_{rot} is the intrinsic maximum rotation velocity (corrected for inclination, $v_{rot} = v_{LOS}/sin(i)$) and σ_0 is the intrinsic velocity dispersion of the rotating disk, related to its thickness. In this work, we define σ_0 as the measured line width in the outer parts of the galaxy, corrected for the instrumental spectral resolution (e.g. Förster Schreiber et al. 2018).

3D-Barolo best-fit results have been obtained following two different approaches. The first one consists of a two-step strategy. First, we tried different azimuthal models spanning a range of disk inclination angles i with respect to the observer (5 to 85° spaced by 5°, with 0° for face-on); during this step, the i parameter is fixed, and the fitting minimization is performed considering the following free parameters: v_{rot}, the rotation velocity, σ, the velocity dispersion, and ϕ, the major axis PA. The disk center is fixed to the position of the nucleus (inferred from registered HST/F160W images; see Paper I). We therefore inferred the disk inclination angle considering the best-fit configuration with minimal residuals, defined using the Eqs. 2 and 3b in Di Teodoro & Fraternali (2015). Then, we run 3D-Barolo with a local normalization, letting it minimize the v_{rot}, σ, ϕ and i parameters. In this second step, the inclination is left free to vary in a few degrees around the best-fit i defined in the previous step. For the second method, we simply run 3D-Barolo with a local normalization, but initialising the inclination to the value derived from the isophote modelling of HST data (Sect. 2.2.2), hence assuming that continuum and narrow Hα have the same geometry. As for the PA measurements, 3D-Barolo fit analysis is performed on the innermost nuclear position, excluding the regions with poor S/N (< 3), for which a Voronoi tesselation would be required in the 3D-barolo modelling.

The resulting best fit plots for I13120 are shown in Fig. 6, while best-fit parameters are reported in Table 2, together with
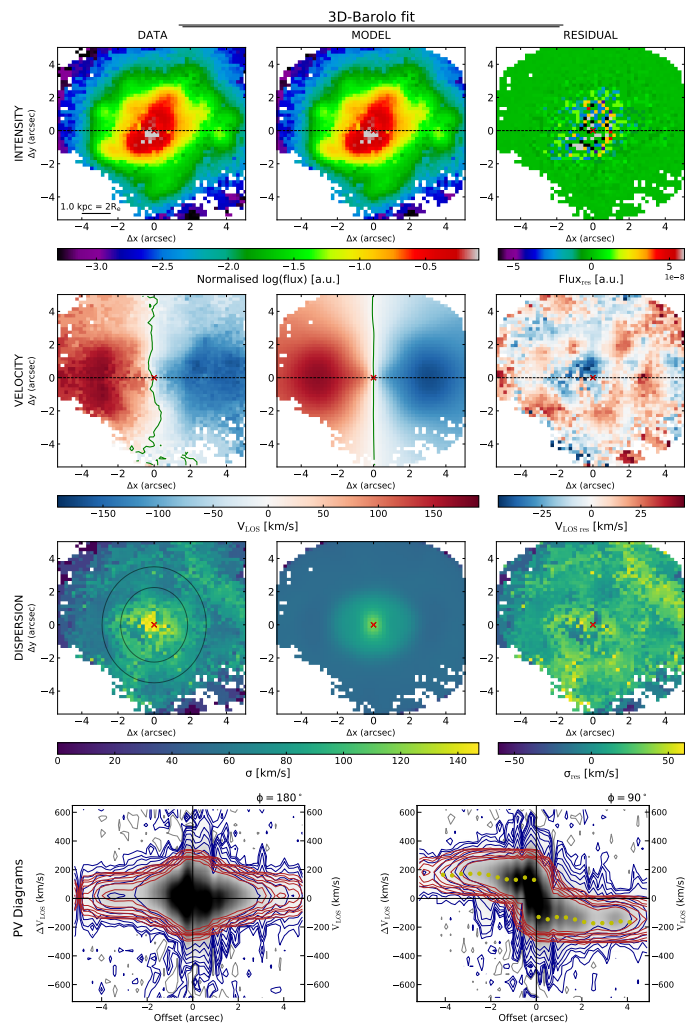

Fig. 6: I13120 narrow Hα 3D-Barolo disk kinematic best-fit of the moment 0, 1 and 2 (first to third rows) and PV diagrams along the minor and major disk kinematic axes (bottom). The black curves in the velocity dispersion map obtained from the data (third row, left panel) identify the region from which σ_0 is extracted. In the PV diagram along the major axis (bottom right) and minor axis (left), data are indicated with a grey-scale map and blue contours, while best-fit model are shown with red contours.

those of the remaining 7 targets with evidence of rotation (see Appendix C for their 3D-Barolo fit analysis). We note that the 3D-Barolo best-fit inclination of I13120 obtained with the two methods, $i_I = 34° ± 3°$ and $i_{II} = 27° ± 3°$, are still consistent with the value we derived from the isophote modelling of HST/F160W data, $i_{morph} = 25° ± 11°$ (Sect. 2.2.2). However, their slightly different i values translate in different rotational velocities; we therefore decided to report in the table the best-fit results obtained with both methods. Similarly, for each target in the table we indicate if both methods provide totally consistent results (I10190 W and I20100 SE) or not (I13120 and IZw1), or alternatively, if the results are obtained from the first (I07251, I12072 and I14348 NE, with no isophote analysis) or the second method only (I17208, with unconstrained i when fitted with the first approach).

The σ_0 values reported in Table 2 are estimated from the narrow Hα velocity dispersion map, as the median value in a radial elliptical annulus which takes care of the disk inclination (as shown in the velocity dispersion panels, see e.g. Fig. 6). This was

Table 2: Hα disk parameters

target	3DB method(s)	i^{3DB} (deg)	ϕ^{3DB} (deg)	v_{rot}^{3DB} (km/s)	σ_0 (km/s)	v_{rot}^{3DB}/σ_0	R_e (kpc)	M_{dyn} ($\times 10^{10}\,M_\odot$)	M_* ($\times 10^{10}\,M_\odot$)
(1)	(2)	(3)	(4)	(5)	(6)	(7)	(8)	(9)	(10)
IZw1	I	47 ± 4	138 ± 9	195 ± 20	35 ± 14	8 ± 3	1.84 ± 0.05† (1.0 ± 0.1)	$3.6^{+0.8}_{-1.0}$	–
	II	38 ± 3	136 ± 8	220 ± 20	32 ± 12	7 ± 4	1.84 ± 0.05† (1.0 ± 0.1)	$4.4^{+0.8}_{-1.0}$	–
I07251	I	45 ± 6	285 ± 6	185 ± 15	80 ± 30	2 ± 1	2.8 ± 0.6* (2.3 ± 0.4)	$7.0^{+2.8}_{-3.4}$	–
I10190 W	I, II	48 ± 4	117 ± 9	210 ± 11	56 ± 10	3 ± 1	2.6 ± 0.1 (2.9 ± 0.3)	$6.5^{+0.9}_{-1.1}$	4
I12072 N	I	48 ± 4	87 ± 6	70 ± 9	85 ± 25	0.8 ± 0.3	2.8 ± 0.6* (1.6 ± 0.3)	$3.5^{+2.2}_{-2.8}$	3.6
I13120	I	34 ± 3	88 ± 8	270 ± 12	58 ± 10	5 ± 1	0.5 ± 0.1 (1.0 ± 0.3)	$1.9^{+0.4}_{-0.5}$	3 ± 0.1
	II	27 ± 3	88 ± 9	315 ± 20	58 ± 10	6 ± 1	0.5 ± 0.1 (1.0 ± 0.3)	$2.5^{+0.6}_{-0.7}$	3 ± 0.1
I14348 NE	I	52 ± 3	185 ± 7	109 ± 8	73 ± 15	1.5 ± 0.3	2.8 ± 0.6* (6.0 ± 0.7)	$3.6^{+1.6}_{-1.9}$*	10.8
I17208	II	47 ± 4	142 ± 5	155 ± 15	70 ± 20	2 ± 1	1.3 ± 0.1 (1.7 ± 0.4)	$2.3^{+0.8}_{-0.9}$	13.5 ± 4.0
I20100 SE	I, II	58 ± 4	287 ± 6	110 ± 10	78 ± 18	1.4 ± 0.3	1.5 ± 0.2 (3.7 ± 0.6)	$2.1^{+0.9}_{-1.1}$	–

Notes. Column (1): Target name. (2): 3D-Barolo fit analysis methodology: 'I' for a two-step strategy, to first constrain the inclination and then all remaining disk parameters, and 'II' for a single-step strategy considering the i^{morph} (Sect. 2.2.2) as initial guess for the inclination. (3): 3D-Barolo disk inclination i. (4): 3D-Barolo kinematic PA of the major axis on the receding half of the galaxy, taken anticlockwise from the North direction on the sky. (5): 3D-Barolo rotation velocity. (6) measured velocity dispersion in the outer part of the galaxy, after subtracting the instrumental resolution (in quadrature). (7): maximum rotation velocity over velocity dispersion. (8): effective radius measurements from Table 1; these values have been preferred to those obtained from the Hα flux map, reported in parenthesis, as less affected by dust obscuration. They are however totally consistent with R_e(Hα), in the range $1 - 2.9$ kpc. The only exceptions are represented by I14348 NE and I20100 SE, which R_e(Hα) are strongly affected by the presence of strong off-nuclear Hα emission. (9): dynamical masses within $2R_e$. (10): (SED-based) stellar masses from Rodríguez Zaurín et al. (2010) and da Cunha et al. (2010). For the former, no uncertainties were reported in the original paper.
(†): R_e from Veilleux et al. (2006), see Sect. 2.2.2. (*): mean R_e of local (U)LIGs, from Bellocchi et al. (2013).

preferred to the (beam-smearing corrected) value that could be inferred from 3D-Barolo, because of the significant fit residuals in the velocity maps, and for consistency with previous works in the literature (see next sections). The use of an annulus region allows us to mitigate the beam-smearing effects or residual outflow contributions, which are higher in the centre than the outside (see e.g. PV diagrams in Fig. 6), and - more in general - remove different contributions which artificially increase (by a ∼ 20%, on average) the velocity dispersion, e.g. due to tidal streams and companion systems. We used these σ_0 values to measure the ratio v_{rot}/σ_0 for all the galaxies with indication of gas rotation (column 7 in Table 2).

It is important to note that our best-fit models have important limitations and systematic uncertainties, and the small formal errors on a parameter do not necessarily imply a good fit (see Neeleman et al. 2021). Both the very simplified disk models and a (possible imprecise) separation between narrow and perturbed Hα components (Sect. 2.2) might be responsible of the significant residuals we observe in the velocity and velocity dispersion maps (e.g. Fig. 6). Nevertheless, our 3D kinematical analysis shows that, on average, this small sub-sample of PUMA systems have a ratio of rotational velocity to velocity dispersion of $v_{rot}/\sigma_0 \sim 1 - 8$. Although slightly lower than that of spiral galaxies in the local Universe ($v_{rot}/\sigma_0 \sim 10$), our values are still comparable with Hα measurements of other low-z (U)LIRGs in the literature (e.g. Bellocchi et al. 2013; Crespo Gómez et al. 2021) and systems at z ∼ 0.5−1 (Rizzo et al. 2021 and references therein). Therefore, 3D-Barolo results provide further indication of rotationally-supported gas motions in these targets.

3.6. Gas velocity dispersion in (U)LIRGs and high-z populations: Dependence on starburstiness

Many theoretical and observational studies suggest that gas in high-z galaxies has larger random motions compared to nearby galaxies: in particular, the ionised gas velocity dispersion goes from ∼ 20 km/s in nearby spirals to ∼ 45 km s^{-1} in massive main

sequence star-forming disk galaxies at z ∼ 2, although with a significant scattering of values (e.g. Übler et al. 2019).

Figure 7, top, shows the narrow Hα velocity dispersion of our rotationally supported PUMA systems (red circles) as a function of the redshift, together with the Übler et al. (2019) evolutionary trend of star-forming galaxies. This trend mostly traces the velocity dispersion evolution of normal MS galaxies (e.g. Übler et al. 2019; Förster Schreiber et al. 2018); we therefore labelled it as $\sigma_{0, MS}$ hereinafter. The σ_0 of our PUMA systems, in the range $30 - 85$ km s^{-1}, are more compatible with - or possibly higher than - those of high-z galaxies rather than nearby spirals. This can be explained taking into account the following arguments. On the one hand, the velocity dispersion increases as natural consequence of the availability of huge gas reservoirs and intense star formation that is taking place in ULIRGs and high-z galaxies (e.g. Lehnert et al. 2009; Arribas et al. 2014; Johnson et al. 2018). On the other hand, both the gravitational instabilities due to the galaxy interactions and the presence of non-circular motions in our PUMA targets can contribute to the σ_0 enhancement with respect to isolated nearby galaxies.

To better investigate the origin of the differences between PUMA systems and normal MS galaxies at different redshifts, in Fig. 7 we report additional individual ionised gas measurements of SB disk galaxies from the literature (see Appendix D for details). Many of them show a significant deviation from the $\sigma_{0, MS}$ evolutionary trend, similar to our PUMA systems.

All these measurements from the literature have been obtained from IFS data; therefore, they are not strongly affected by beam-smearing effects and other systematics that tend to overestimate the intrinsic dispersion (see discussion in Übler et al. 2019). We also stress here that all selected individual sources are disk galaxies. This ensures relatively small contribution of outflows in the velocity dispersion measurements, which incidence increases with SFR and AGN activity (e.g. Cicone et al. 2016; Villar Martín et al. 2020). A few additional caveats should be kept in mind regarding this compilation of sources: all of them are presented as SB galaxies in the original papers, but we note that i) there is no rigorous definition of a SB galaxy, but sev-
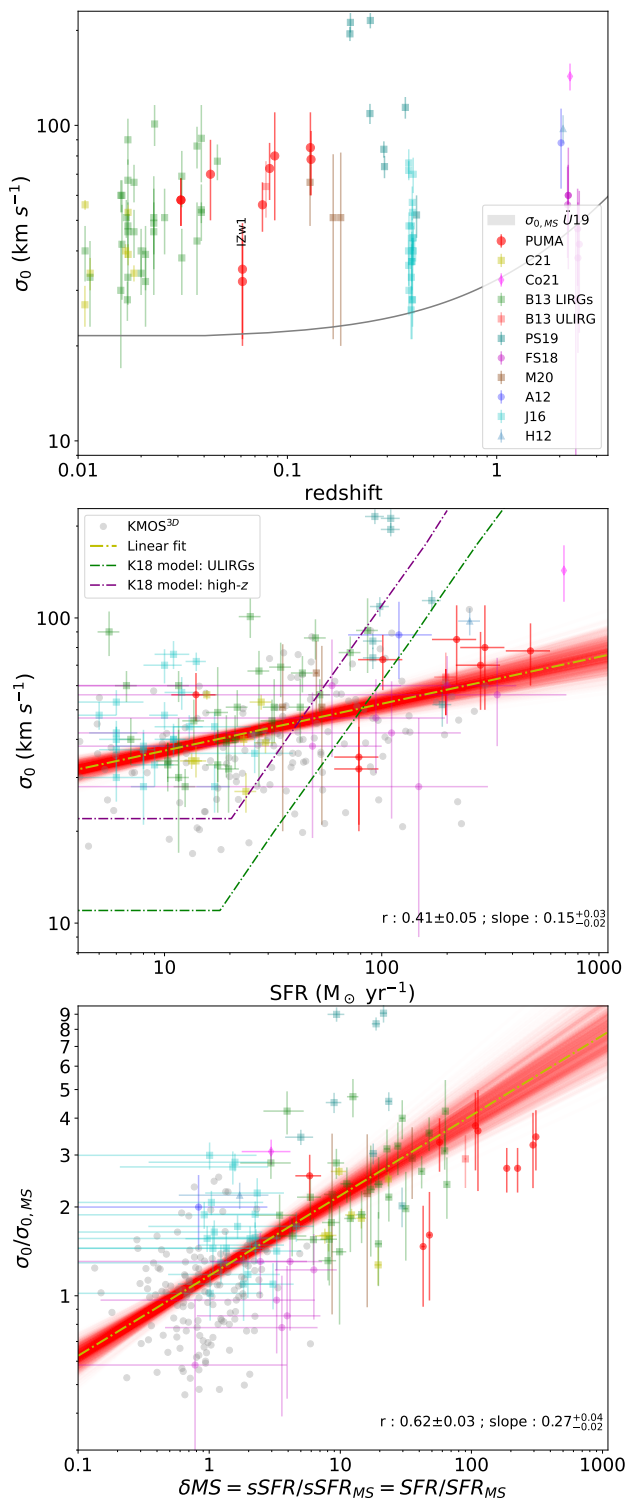
Fig. 7: *Top*: Velocity dispersion σ_0 as a function of z for PUMA subsample (red dots) and other individual ionised gas measurements from the literature, distinguishing between the different samples presented in Appendix D, as labeled. The Übler et al. (2019) evolutionary trend of MS galaxies is shown with a solid curve (shaded area: 1σ scatter around the average trend). *Middle*: σ_0 as a function of the SFR, for all targets already reported in the first panel, and the KMOS^{3D} galaxies (grey points; Übler et al. 2019). K18 models and a linear fit (with scatter) are also reported, as labeled. *Bottom*: σ_0 normalised to the evolutionary trend of MS galaxies as a function of δMS for all targets already reported above. A linear fit is also reported.

eral different criteria are often used, and ii) especially at high-z, stellar mass and SFR measurements can be highly uncertain, depending on the availability of multi-wavelength information. This aspect is further discussed below.

3.6.1. The $\sigma_0 - SFR$ correlation

Most of the galaxies presented in Fig. 7, top, significantly deviate from the $\sigma_{0, MS}$ evolutionary trend. In order to understand if this deviation is due to the extreme SFR in these systems, we show in Fig. 7, middle, the velocity dispersion σ_0 as a function of the SFR, for all the targets already mentioned, in addition to the sample of normal MS galaxies used to derive the $\sigma_{0, MS}$ trend (Übler et al. 2019). All SFR measurements of SB reported in the figure are obtained from IR luminosities (as reported in the original papers, or using the Kennicutt 1998 relation, assuming the Chabrier IMF). For the PUMA targets, we considered the nuclear IR luminosities reported in Paper II, table 7; for the binary systems, the fraction of the IR luminosity assigned to each nucleus is based on their relative ALMA continuum fluxes. We observe a relatively poor correlation (Spearman rank correlation coefficient 0.4), reasonably due to a bias selection: a more clear correlation is in fact observed when combining samples of galaxies covering a larger dynamical range, i.e. also including local MS galaxies (e.g. Yu et al. 2019; Varidel et al. 2020). By performing a linear regression fit we derive

$$log(\sigma_0) = (0.15^{+0.03}_{-0.02}) \times log(SFR) + (1.46 \pm 0.04), \quad (1)$$

compatible (within 1σ) with Arribas et al. (2014) previous results, obtained from a sample of (U)LIRGs observed with the optical spectrograph VIMOS. We compare this fit with the model predictions by Krumholz et al. (2018), for both high-z galaxies and local ULIRGs (dash-dotted lines in Fig. 7, middle). The slight differences between the two theoretical curves in the figure are due to the distinct ISM physical conditions of these two classes of sources (see Table 3 in Krumholz et al. 2018). These models explain the observed slow increase in σ_0 as a function of SFR in the range $[10^{-3}, 10]$ M$_\odot$ yr^{-1}, followed by a steeper increase up to 10s km s^{-1} considering two different regimes. The σ_0 floor is due to stellar feedback processes, while at higher SFR the velocity dispersion is regulated by gravitational turbulence. We note that the comparison between these theoretical curves and our collected data is strongly limited by caveats. To begin, all SB galaxies in our plot are disk galaxies: this could result in the exclusion of all targets with more extreme (i.e. higher) σ_0. The next problem is that the Bellocchi et al. (2013) and PUMA velocity dispersion measurements in this plot are derived from the narrow Hα, i.e. after removing the more extreme kinematic components. As shown in Figs. A.1-A.19 and Fig. B, significantly higher velocity dispersion (up to several 100s km s^{-1}) is measured in the total Hα line profiles of our PUMA galaxies, reasonably associated with extended outflows and streaming motions. Finally, the ISM of (U)LIRGs and high-z SB galaxies might not be in vertical pressure nor energy balance, as assumed in Krumholz et al. (2018) models: instead, their velocity dispersion might be strongly affected by non-circular motions. Specifically, these σ_0 measurements might not be dominated by the turbulent component, that is relevant for a comparison with the SFR (e.g. Bacchini et al. 2020).

3.6.2. The $\sigma_0/\sigma_{0, MS} - \delta MS$ correlation

In the σ_0-SFR plane, local (U)LIRGs and high-z galaxies tend to occupy the same region, regardless of their intrinsic differ-

ence in terms of morphology, gas fraction and starburstiness. In order to distinguish between normal MS and SB galaxies, we show in Fig. 7, bottom, the velocity dispersion σ_0 normalised to $\sigma_{0,\ MS}$ (solid line in the top panel; Übler et al. 2019) as a function of the starburstiness $\delta MS = sSFR/sSFR|_{MS}$ for all targets already reported in the previous panels. The $sSFR|_{MS}$ is derived from the Speagle et al. (2014) relation, starting from the available stellar mass measurements from the literature for Johnson et al. (2016), Förster Schreiber et al. (2018), Molina et al. (2020), Cochrane et al. (2021), and KMOS^{3D} individual targets; stellar masses of LIRGs and ULIRGs from this study, from Bellocchi et al. (2013), Pereira-Santaella et al. (2019) and Crespo Gómez et al. (2021), are instead derived from the dynamical mass estimates, assuming $M_* = (1 - f_{gas}) \times (1 - f_{DM}) \times M_{dyn}$, where f_{gas} and f_{DM} are the gas and dark matter fractions[4], respectively, and M_{dyn} is the dynamical mass within $2R_e$ (see next section). For the gas fraction, we considered a conservative $f_{gas} = 0.1$ (Isbell et al. 2018; higher f_{gas} values would further increase their δMS). This gas fraction is consistent with the estimate we obtain considering the molecular gas mass inferred by ALMA data (Paper II; Lamperti et al., in prep) and the M_* measurements available for a few PUMA targets (see Table 2), $\bar{f}_{gas} = 0.11 \pm 0.05$. For the dark matter fraction (within $2R_e$) we assumed $f_{DM} = 0.26$, defined as $1 - M_{bar}/M_{dyn}$, with $M_{bar} = M_* + M_{gas} = M_*/(1 - f_{gas})$. The f_{DM} estimate was derived for the PUMA and Johnson et al. (2016) SB galaxies for which stellar masses are available, and considering the dynamical masses within $2R_e$ (see Sect. 3.7). Because of these assumptions, we considered a factor 3 uncertainties for the stellar mass measurements of (U)LIRGs. These uncertainties, however, play a minor role in the derived δMS: at low-z, the MS has a soft slope, and normal and massive MS galaxies have similar SFRs (e.g. at $z \sim 0.1$, galaxies of 10^{10} and 10^{11} M$_\odot$ have $SFR|_{MS} \sim 1$ and ~ 3.5 M$_\odot$ yr^{-1}, respectively); on the other hand, local (U)LIRGs have much higher SFRs, from 10s to 100s M$_\odot$ yr^{-1}, and therefore δMS of the order of $10 - 100$. Finally, for the Alaghband-Zadeh et al. (2012) and Harrison et al. (2012) high-z galaxies we assumed that $M_* = 10^{11}$ M$_\odot$, following Harrison et al. (2012).

Figure 7, bottom, shows a clear correlation between $\sigma_0/\sigma_{0,\ MS}$ and δMS (Spearman rank correlation coefficient 0.6), suggesting that SB galaxies tend to have higher velocity dispersion than normal galaxies at given z and stellar mass. A tentative evidence of such correlation was already reported by Wisnioski et al. (2015), for the KMOS^{3D} galaxies at $z \sim 2$, and by Varidel et al. (2020), for nearby MS galaxies of the SAMI survey, but the lack of dynamical range in terms of starburstiness in these surveys maintained the correlation at low significance level (see also Figs. 15-16 in Übler et al. 2019).

By performing a linear regression fit, we derived

$$log(\sigma_0/\sigma_{0,\ MS}) = (0.27^{+0.04}_{-0.02}) \times log(\delta MS) + (0.07^{+0.02}_{-0.01}). \quad (2)$$

Given the correlation between σ_0 and SFR (e.g. Varidel et al. 2020) and the tight inter-relationship between δMS and f_{gas} (e.g. Wisnioski et al. 2015; Tacconi et al. 2020), it is unsurprising that the starburstiness correlates with the excess in the velocity dispersion with respect to MS galaxies. The positive slope of ~ 0.27 is inconsistent with the one observed between f_{gas} and δMS, +0.5 (Tacconi et al. 2020), suggesting that complex interactions between different physical drivers are responsible of the correlation observed in Fig. 7 (bottom). As a final check, we studied the correlation between σ_0 and v_{rot}, as well as between

---

[4] In this work, we define $f_{gas} = M_{gas}/M_{bar}$, with $M_{bar} = (M_* + M_{gas})$, and $f_{DM} = M_{DM}/M_{dyn}$.

$\sigma_0/\sigma_{0,\ MS}$ and v_{rot}, obtaining Spearman coefficients of ~ -0.2 (with p-value ~ 0.05); this shows that not even v_{rot} can have a significant role in determining the increase in the velocity dispersion of SB galaxies.

The strong correlation $\sigma_0/\sigma_{0,\ MS} - \delta MS$ suggests that the SFR of galaxies above the MS is taking place in an ISM significantly more unsettled than in normal (i.e. MS) galaxies. This is likely due to the presence of interactions and mergers which enhance SFR while simultaneously increase the velocity dispersion of the ISM. The absence of a strong correlation between SFR and elevated velocity dispersion in star-forming clumps both in local (U)LIRGs and high-z SFGs (Arribas et al. 2014; Genzel et al. 2011) further suggests that the extreme dispersion cannot be simply related to the strong SFR in these systems.

Our arguments are consistent with the parsec-resolution hydrodynamical simulations of major mergers presented by Renaud et al. (2014): they found that the increase of ISM velocity dispersion precedes the star formation episodes. Therefore, this enhancement is not a consequence of stellar feedback but instead has a gravitational origin. In this scenario, δMS can be interpreted as a tracer of the strength of gravitational torques: stronger gravitational torques during the interactions lead the gas to flow inwards, both increasing the velocity dispersion and the efficiency in converting gas into stars.

We finally mention that AGN outflows, which are ubiquitous in these systems (Paper I; Paper II), can also contribute to increase the velocity dispersion of the disks, as suggested by high-resolution hydrodynamic simulations (e.g. Wagner et al. 2013; Cielo et al. 2018).

A more detailed investigation of the physical meaning of the correlations reported in Fig. 7 goes beyond the purpose of this study; here we just stress that, by selecting a (relatively small) sample of MS and SB disk galaxies in the redshift range $0.03 - 2.6$, a more significant correlation is observed between $\sigma_0/\sigma_{0,\ MS}$ and δMS rather than between σ_0 and SFR. We argue that this result might be even more evident considering the entire population of (U)LIRGs (i.e. without excluding targets with no evidence of rotating disk; see e.g. Table 1), and measuring the velocity dispersion without excluding possible contribution from outflows and streaming motions (see Figs. A.1-A.19).

3.7. Dynamical masses

In this section we derive the dynamical masses of our PUMA sub-sample, and compare them with those of other (U)LIRGs from the literature. Assuming that the source of the gravitational potential is spherically distributed, we can estimate the dynamical mass within a radius R as:

$$M_{dyn} = \frac{v^2_{circ}}{G}R = 2.33 \times 10^5 v^2_{circ} R, \quad (3)$$

where G is the gravitational constant, v_{circ} is the circular velocity in km/s, and R is given in kpc.

We used the near-IR continuum $2R_e$ as the radius to calculate M_{dyn}, which for an exponential profile contains 85% of the total flux. The effective radius of I10190 W, I13120 and I17208 is computed with the Isophote package of Astropy (Sect. 2.2.2); IZw1 R_e is instead taken from Veilleux et al. (2006), who performed multi-component two-dimensional image decomposition to separate the host galaxy from its bright active nucleus; for the remaining three targets, we adopted the ULIRGs average R_e derived by Bellocchi et al. (2013), as the presence of nearby nuclei

(I07251 and I12072) and strong tidal features (I14348 NE) do not allow us to model the continuum with isophotal ellipses.

To infer the circular velocity we consider both the rotation and dispersion motions traced by the narrow Hα. In particular, we included the asymmetric drift term, which represents an extra component due to the dispersion of the gas around the disk of the galaxy,

$$v_{circ}^2 = v_{rot}^2 + \eta \sigma^2. \tag{4}$$

The term η is a constant and can vary between approximately 1.5 and 6, depending on the mass distribution and kinematics of the galaxy: higher values indicate higher turbulence in the ISM of a rotating disk (Neeleman et al. 2021). We assumed $\eta = 3$, following Dasyra et al. (2006), which is very close to the value expected for an exponential, turbulent pressure-supported disk ($\eta = 3.4$), and considered an uncertainty of 1.5 to take into account the large range of possible values. We note that, on average, our dynamical masses would be a factor 1.15 lower (1.32 higher) assuming $\eta = 1.5$ (6).

The assumption of a spherically distributed ISM is at odds with that we used in Sect. 3.5 to measure the rotational velocities in our systems. In order to account for this, following Neeleman et al. (2021), we conservatively increased the dynamical mass uncertainty by 20% toward lower masses. This corresponds to consider that the effective total mass distribution falls somewhere in between a thin disk and a sphere.

The measured dynamical masses of our PUMA systems range from ~ 2 to $\sim 7 \times 10^{10}$ M$_\odot$, consistent with the median value derived by Bellocchi et al. (2013) for ULIRG systems, 4.8×10^{10} M$_\odot$, confirming that ULIRGs are intermediate mass systems like previously suggested (i.e., Colina et al. 2005; Rodríguez Zaurín et al. 2010).

In this final part, we further discuss about the dark matter fraction reported in the previous section, and defined as $f_{DM} = 1 - M_{bar}/M_{dyn}$. Using a sub-sample of 27 SB disk galaxies with available M_* measurements, and assuming $f_{gas} = 0.1$, we obtained a median value $f_{DM} = 0.26$. We note however that, for a few sources (6/27, mostly from the PUMA sample), $M_* > M_{dyn}$ (Table 2; see also Table 6 in Rodríguez Zaurín et al. 2010). This can either suggest that the systems are not relaxed (due to the interaction/mergers) and M_{dyn} is unreliable, or that M_* measurements have high uncertainties. As the M_{dyn} estimates are in agreement with previous works, and because of the fact that for binary PUMA systems in Table 2 the available M_* measurements are obtained without separating the contribution of the merging galaxies, we favour the second interpretation, i.e. that M_* measurements are highly uncertain though a combination or both may also be possible. These arguments led us to consider significant (factor of 3) uncertainties in the determination of the stellar masses for the entire sample of local (U)LIRGs, required to estimate their δMS. The conclusions reported in the previous section are however not affected by these uncertainties, because of extreme SFR in (U)LIRGs targets.

4. Summary and conclusions

The project called Physics of ULIRGs with MUSE and ALMA (PUMA) is a survey of 25 nearby ULIRGs observed with MUSE and ALMA. This is a representative sample that covers the entire ULIRG luminosity range, and it includes a combination of systems with AGN and SB nuclear activity in (advanced) interacting and merging stages. Paper I presents the first MUSE results on the spatially resolved stellar kinematics and the incidence of ionized outflows in nuclear spectra; Paper II analyzes

high-resolution (400 pc) ~ 220 GHz continuum and CO(2–1) ALMA observations to constrain the hidden energy sources of ULIRGs. In this paper, we investigated the presence of ionised gas rotational dynamics in PUMA targets, to understand if, as predicted by models, rotation disks can be preserved during the merging process (or rapidly regrown after coalescence) and, if so, which are their main properties. Our results are summarised below.

(a) We presented the spatially resolved Hα flux and kinematic maps for the entire PUMA sample, obtained from multi-component Gaussian fit analysis (Fig. A.1- A.19). Irregular large scale ionized gas velocity fields associated with tidally-induced motions and outflows are found in almost all targets; Hα velocities ($v50$) up to $\sim \pm 300$ km s^{-1} are detected in the MUSE FOV, while Hα line-widths $W80$ range from ~ 100 to ~ 1500 km s^{-1}. [NII] (and [OIII]) line transitions are even more affected by perturbed motions, as tidal streams and outflows.

(b) We studied the Hα kinematics to infer the presence of rotating disk signatures. A kinematic decomposition is performed by selecting in the $\Delta V_j - FWHM_j$ plane all best-fit Gaussian components with relatively small velocities, and constructing new narrow Hα data cubes. In these newly generated data cubes the emission associated to gas components with extreme velocities (likely due to outflows and/or tidally driven flows) is minimized.

(c) By studying the gas kinematics along the major axes of our galaxies in the innermost regions ($\sim 5 - 20$ kpc), we found that 27% (8/29) individual nuclei are associated with disk-like motions. This has to be considered as a lower limit, as the presence of vigorous winds and gravitational torques, as well as observational limitations (in terms of spatial and spectral resolution, and S/N), limit our capabilities in isolating more regular, disk-like kinematics through a multi-component Gaussian fit decomposition. This is supported by the fact that 5 merger remnants in our sample present stellar disk motions but highly perturbed gas kinematics. Indeed, the incidence of ionised gas rotating disks is a factor $\lesssim 2$ smaller than that of stellar disk-like motions (Paper I). This is possibly suggesting that i) we are actually missing a significant fraction of sources with gas rotation because of the above mentioned limitations, or ii) gas component is more affected by winds and gravitational interactions and the probability of preserving a gas disk is lower than that of a stellar disk. In both instances, our results show that, as predicted by models, rotation disks can be preserved during the merging process and/or rapidly regrown after coalescence.

(d) For the 8 galaxies with evidence of disk-like motions, we modelled the narrow Hα data cubes with 3D-Barolo, and derived rotational velocities $v_{rot} \in [70-300]$ km s^{-1}. By combining them with the measured velocity dispersion σ_0 ($\in [30 - 80]$ km s^{-1}), we derive v_{rot}/σ_0 values in the range 1-8, providing further indication of rotationally supported gas motions in these ULIRGs. We also derived their M_{dyn}, obtaining values in the range $(2 - 7) \times 10^{10}$ M$_\odot$, consistent with M_{dyn} of other ULIRGs in the literature.

(e) We compared the narrow Hα velocity dispersion σ_0 of our 8 PUMA disk galaxies with those of other SB and normal MS disk galaxies at low and high-z. We found that all SB galaxies tend toward higher σ_0 values compared to MS galaxies at the same redshift. Interestingly, when we normalise σ_0 to the value expected for MS galaxies (at the same z), considering the Übler et al. (2019) evolutionary trend $\sigma_{0, MS}$, we found a significant correlation between $\sigma_0/\sigma_{0, MS}$ and the starburstiness δMS. In particular, SB galaxies display up to a factor ~ 4 higher velocity dispersion than normal MS galaxies at same redshift. The rela-

tively poor correlation between σ_0 and the SFR (Fig. 7, middle) suggests that stellar activity cannot be the main responsible for the σ_0 enhancement observed in SB galaxies, and other mechanisms possibly related to interactions and mergers should be taken into account (see e.g. Renaud et al. 2014).

We note however that most of the SB galaxies at $z \gtrsim 0.4$ collected from the literature are consistent with $\delta MS = 1$ once homogeneous recipes are used to derive the SFR, and measurement uncertainties are taken into account. As a result, the correlation reported in the figure is mostly driven by the comparison between $z \sim 0.03 - 0.4$ (U)LIRGs and KMOS^{3D} MS galaxies at $z \sim 0.6 - 2.6$. This makes highly desirable a further investigation of gas dynamical conditions in SB galaxies at $z > 0.4$. The JWST NIRSpec IFS, with its wide spectral range (from 0.6 to 5.3 μm) and sub-arcsec resolution, will allow a comprehensive characterisation of the ionised gas dynamical conditions in such systems.

References

Alaghband-Zadeh S.; Chapman S. C.; Swinbank, A. M. et al., 2012, MNRAS, 424, 2232

Allen M.G., Groves B.A., Dopita M.A. et al. 2008, ApJS, 178, 20A

Arribas, S., Colina, L., Bellocchi, E., et al. 2014, A&A, 568, 14A

Astropy Collaboration, Price-Whelan, A. M., Sipocz, B. M., et al. 2018, AJ, 156, 123

Bacchini C., Fraternali F., Iorio G., et al., 2020, A&A, 641, 70

Bae, H. J. & Woo, J. H. 2014, ApJ, 795, 30

Barrera-Ballesteros, J. K., García-Lorenzo, Falcón-Barroso, J., et al. 2015, A&A, 582, 21

Bellocchi, E., Arribas, S., Colina, L., Miralles-Caballero, D. 2013, A&A, 557, 59

Bradley, L., Sipocz, B., Robitaille, T., et al. 2016, Photutils: Photometry tools, Astrophysics Source Code Library [record ascl:1609.011]

Bullock J. S., Stewart K. R., Purcell C. W., 2009, in Andersen J., BlandHawthorn J., Nordstrom B., eds, IAU Proc. Symp. 254, The Galaxy Disc in Cosmological Context. Cambridge Univ. Press, Cambridge, p. 85

Cappellari, M., Copin, Y. 2003, MNRAS, 342, 345

Cappellari, M. & Emsellem, E. 2004, PASP, 116, 138

Cappellari, M. 2017, MNRAS, 466, 798

Cazzoli S., Arribas S., Colina L., et al. 2014, A&A, 569, 14

Chen YM, Shi Y., Tremonti C., et al., 2016, Nat. Commun., 7, 13269

Cicone, C., Maiolino, R., Marconi, A., 2016, A&A, 588, 41

Cielo S., Bieri R., Volonteri M., et al. 2018, MNRAS, 477, 1336

Cochrane R. K., Best, P. N., Smail, I., et al. 2021, MNRAS, 503, 2622

Colina, L., Arribas, S., Monreal-Ibero, A. 2005, ApJ, 621, 725

Costantin L., Méndez-Abreu J., Corsini E. M., et al. 2017, A&A601, 84

Costantin L., Corsini E. M., Méndez-Abreu J., et al. 2018, MNRAS, 481, 3623

Cox T. J., Dutta S. N., Di Matteo T., et al., 2006, ApJ, 650, 791

Crespo Gómez A., Piqueraz López J., Arribas S., et al., 2021, A&A, 650, A149

da Cunha, E., Charmandaris, V., Díaz-Santos, T., et al., 2010, A&A, 523, 78

Dasyra, K. M., Tacconi, L. J., Davies, R. I., et al. 2006, ApJ, 651, 835D

Dekel, A., Birnboim, Y., Engel, G., 2009, Nature, 457, 451

Di Teodoro E. M., Fraternali F., 2015, MNRAS, 451, 3021

Duc, P.-A., Mirabel, I. F., & Maza, J. 1997, A&AS, 124, 533

Elbaz, D., Dickinson, M., Hwang, H. S., et al. 2011, A&A, 533, A119

Fischer T.C., Crenshaw D.M., Kraemer S.B. & Schmitt H.R. 2013, ApJS, 209, 1

Förster Schreiber, N. M., Renzini, A., Mancini, C., et al. 2018, ApJS, 238, 21

Gaia Collaboration 2018, A&A, 616, 1G

Genzel, R., Newman, S., Jones, T., et al. 2011, ApJ, 733, 101

Governato, F., Brook, C. B., Brooks, A. M. et al. 2009, MNRAS, 398, 312

Haan, S., Surace, J. A., Armus, L., et al., AJ, 141, 100

Hammer, F., Flores, H., Yang, Y. H., et al., 2009, A&A, 496, 381

Harrison C.M., Alexander D.M., Swinbank A.M. et al. 2012, MNRAS, 426, 1073

Harrison, C. M., Alexander, D. M., Mullaney, J. R., et al. 2016, MNRAS, 456, 1195

Hopkins, P. F., Cox, T. J., Younger, J. D., Hernquist, L. 2009, ApJ, 691, 1168

Hopkins, P. F., Cox, T. J., Hernquist, L., et al., 2013, MNRAS, 430, 1901

Isbell, Jacob W.; Xue, Rui; Fu, Hai, 2018, ApJ, 869, 371

Johnson H.L., Harrison C.H., Swinbank A.M., et al., 2016, MNRAS, 460, 1059

Johnson H. L., Harrison C. M., Swinbank A. M., et al., 2018, MNRAS, 478, 5076

Kennicutt R.C., 1998, ARA&A, 36, 189K

Kereŝ D., Katz N., Weinberg D. H., Davé R., 2005, MNRAS, 363, 2

Kim, D.-C., & Sanders, D. B. 1998, ApJS, 119, 41

Kim, D.-C., Evans, A. S., Vavilkin, T., et al. 2013, ApJ, 768, 102

Krajnovic D., Cappellari M., de Zeeuw P.T, Copin Y., 2006, MNRAS, 802, 787

Krumholz, M. R., Burkhart, B., Forbes, J. C., et al. 2018, MNRAS, 477, 2716

Lehnert M. D., Nesvadba N. P. H., Le Tiran L., et al., 2009, ApJ, 699, 1660

Leung, T. K. D., Riechers, D. A., Baker A. J., et al., 2019, ApJ, 871, 85

Liu G., Zakamska N. L., Greene J. E., Nesvadba N., Liu X., 2013b, MNRAS, 436, 2576

Medling, A. M., U, V., Guedes, J., et al. 2014, ApJ, 784, 70

Molina, Juan; Ibar, Edo; Godoy, Nicolás et al. 2020, A&A, 643, 78

Mingozzi, M., Cresci, G., Venturi, G., et al. 2019, A&A, 622, 146

Neeleman M., Novak M., Venemans B.V., et al., 2021, ApJ, 911, 141

Pereira-Santaella, M., Rigopoulou, D., Magdis, G. E., et al. 2019, MNRAS, 486, 5621

Pereira-Santaella, M., Colina L., García-Burillo S., et al., 2021, A&A, 651, 42

Perna, M., Curti, M. Cresci, G., et al. 2018, A&A, 618, 36

Perna, M., Cresci, G., Brusa, M., et al. 2019, A&A, 623, 171

Perna, M., Arribas, S., Catalán-Torrecilla, C., et al. 2020, A&A, 643, 139

Perna, M., Arribas, S., M. Pereira Santaella, et al. 2021, A&A, 646, 101

Privon, G., Aalto, S., Falstad, N., et al., 2016, ApJ, 835, 213

Renaud, F., Bournaud, F., Kraljic, K., Duc, P.-A., 2014, MNRAS, 442, 33

Rizzo F., Vegetti S., Fraternali, F., et al., 2021, arXiv:2102.05671

Robertson, B., Bullock, J. S., Cox, T. J., et al. 2006, ApJ, 645, 986

Robertson B. E., Bullock J. S., 2008, ApJ, 685, 27

Rodriguez-Gomez, Vicente; Sales, Laura V.; Genel, Shy, et al. 2017, MNRAS, 467, 3083

Rodríguez Zaurín, J., Tadhunter, C. N., González Delgado, R. M. 2010, MNRAS, 403, 1317

Sanders, D. B., Soifer, B. T., Elias, J. H., et al. 1988, ApJ, 325, 74S

Sanders, D. B., Mazzarella, J. M., Kim, D. C., et al. 2003, AJ, 126, 1607

Sánchez Almeida, J., Elmegreen, B. G., Muñoz-Tuñón, C., Elmegreen, D. M. 2014, A&ARv, 22, 71

Schaye, J., Dalla Vecchia, C., Booth, C.M. et al. 2010, MNRAS, 402, 1536

Scharwächter, J., Eckart, A., Pfalzner, S. et al. 2007, A&A, 469, 913

Schwarz, G., 1978, Ann. Stat., 6, 461

Scoville, N.Z., Yun M.S., Bruant P.M. 1997, ApJ, 484, 702

Sijacki D., Vogelsberger M., Genel S. et al. 2015, MNRAS, 452, 575S

Silk, J. 2013, ApJ, 772, 112S

Smits, D. P. 1996, MNRAS, 278, 683

Springel V., Di Matteo T., Hernquist L., 2005, ApJ, 620, 79

Springel V., Hernquist L., 2005, ApJ, 622, 9

Sparre, Martin; Springel, Volker, 2017, MNRAS, 470, 3946

Speagle J.S., Steinhardt C.L., Capak P.L., Silverman J.D. 2014, ApJS, 214. 15S

Sturm, E., González-Alfonso, E., Veilleux, S., et al. 2011, ApJ, 733, L16

Tacconi, L. J., Genzel, R., Sternberg, A, ARA&A, 58, 157

Tadaki, K., Iono, D., Yun, M. S., et al., 2020, ApJ, 889, 141

Tan, Q.-H., Gao, Y., Kohno, k., et al., 2019, ApJ, 887, 24

Übler H., Genzel R., Wisniski E., et al., 2019, ApJ, 880, 48

Ueda, J., Iono, D., Yun, M. S., et al. 2014, ApJS, 214, 1

Valdes, F., Gupta, R., Rose, J.A., et al. 2004, ApJS, 152, 251

Varidel, M. R., Croom, S. M., Lewis, G. F., et al. 2020, MNRAS, 495, 2265

Veilleux, S., Kim, D.-C., & Sanders, D. B. 2002, ApJS, 143, 315

Veilleux, S., Kim, D.-C., Peng, C. Y., et al. 2006, ApJ, 643, 707

Villar Martín, M., Perna, M., Humphrey, A., et al. 2020, A&A, 634, 116

Wagner A. Y., Umemura M., and Bicknell G. V., 2013, ApJ, 763, 18

Willick J.A., Courteau, S., Faber S.M., et al., 1997, ApJS, 109, 333

Wisnioski E., Förster Schreiber N. M., Wuyts S., et al. 2015, ApJ, 799, 209

Woo, J., H., Bae, H., J., Son, D., & Karouzos, M. 2016, ApJ, 817, 108

Yu, X., Shi Y., Chen, Y., 2019, MNRAS, 4463, 4472

Appendix A: Multi-component Gaussian fit results

Appendix B: Position-Velocity diagrams

In Fig. B.1 we show the comparison between the (total and narrow) Hα and stellar velocities along their kinematic major axis, for all targets for which we can observe a clear velocity gradient (and measure a PA^{kin}) together with a peak in the velocity dispersion diagram at the position of the nucleus for at least one component (i.e. gas or stars). The nuclear positions are inferred from registered HST/F160W images (Paper I). The PV plots show only a small portion of the total extension of the ULIRG systems, in order to exclude the contribution from tidal tails, extended outflows or second nuclei, and better identify rotation-like signatures.

The major axis PA^{kin} measurements have been obtained with the python PaFit package (Krajnovic et al. 2006), for both stellar and gas kinematics (columns 5 and 6 in Table 1). The difficulty in measuring reliable PA^{kin} and obtaining regular velocity profiles, led to the exclusion of the following systems: I07251 E and W, I09022, I11095, I12072 S, I13451 E and W, 19297 S, 20100 NW, I22491 E and W.

For the sources for which the gas and stellar major axes agree within the errors, the PV diagrams have been extracted considering a PA^{kin} equal to the weighted mean of PA$^{kin}_{gas}$ and PA$^{kin}_*$, with the weighting factors equal to the inverse of the quadratic uncertainty on the PA^{kin} measurements; for those sources for which no PA^{kin} measurement can be obtained for the gas, we considered the PA$^{kin}_*$ (I01572, I05189, I19297 N, I19542); vice versa, PA$^{kin}_{gas}$ has been chosen when the stars do not show a clear velocity gradient (I07251 E, I22491 E). Finally, for those sources with different stellar and gas kinematics (I10190 E, I14348 NE, I16090, I20087 and I20100 SE) we extracted the velocity profiles along different PAs.

Before briefly discussing the PV diagrams of individual targets shown in the figure, we note that a clear but shallow velocity gradient (i.e. with $\delta v \ll 100$ km s^{-1}) could translate in a flat σ profile under the MUSE observing conditions (i.e. with an angular resolution $\approx 0.6''$). This would determine the exclusion of disk-like candidates, according to two selection criteria mentioned at the beginning of this section. However, most of PUMA individual systems show $\delta v \gtrsim 100$ km s^{-1} (see Table 1); the few systems with lower δv (in particular, the gas component in I00188, I22491 E, I14348 SW and I14378) also present disturbed kinematics, excluding the presence of disks even in these conditions.

Notes on individual targets in Fig. B.1:

I00188 shows a regular gradient in V_* and a peak in σ_* at the position of the nucleus, as expected for rotation-dominated kinematics; on the other hand, the narrow Hα velocity profiles is irregular, while its velocity dispersion is close to ~ 110 km/s along the entire extension of the major axis, indicating highly perturbed gas kinematics.

IZw1 The Hα in the central pixel is saturated; this translates in a gap in the PV slices shown in the figure. The presence of strong Sy1 emission also prevents us to correctly infer proper V_* and σ_* measurements in the vicinity of the nucleus; in particular, the σ_* values might be strongly overestimated.

I01572 As for IZw1, the presence of a strong Sy1 prevents us to properly infer stellar velocity and velocity dispersion in the vicinity of the nucleus. Moreover, the gas kinematics are strongly disturbed by the nuclear outflow and tidal motions.

I05189 shows a clear gradient in V_* and a peak in σ_* at the position of the nucleus, as expected for rotation-dominated kine-

matics; on the other hand, the narrow Hα velocity profiles is irregular, while its velocity dispersion is close to ~ 110 km/s along the entire extension of the major axis, indicating highly perturbed gas kinematics.

I07251 presents disk-like motions, but with a kinematic centre not coincident with the position of either the two nuclei of this interacting system (see also Fig. C.2, top panels). The PV diagrams presented in Fig. B have been therefore extracted considering the kinematic centre obtained from the 3D-Barolo analysis.

I10190. This system shows two rotating disks associated with the two nuclei, separated by ~ 7.2 kpc. However, both the stellar and gas kinematics in the vicinity of the E nucleus are strongly affected by the presence of the W system motions.

I12072 This source presents two nuclei, at a projected distance of 2.3 kpc. Disk-like motions are presumably associated with the N nucleus. Broadly regular PV diagrams are observed for both stellar and gas components.

I13120 This target is extensively presented in the main text of this work.

I14348 is an interacting ULIRG with two nuclei, at a projected distance of ~ 5 kpc. The NE nucleus presents broadly regular PV diagrams for both gas and stellar components; the SW nucleus presents broadly regular stellar kinematics, and more irregular gas motions due to the presence of a strong outflow.

I14378 shows a clear gradient in V_* and a peak in σ_* at the position of the nucleus, as expected for rotation-dominated kinematics; on the other hand, the narrow Hα velocity profiles is irregular, and $\sigma_{gas} \approx 90$ km/s along the entire extension of the major axis indicates highly perturbed gas kinematics.

Arp220 shows a broadly regular velocity gradient in both gas and stellar components (see also Scoville et al. 1997). However, the presence of the two nuclei with distinct rotation features on scales of ~ 100 pc (at a distance of ~ 370 pc), and a kpc-scale, wide-angle outflow prevents a detailed characterisation of the gas kinematics in this system (see e.g. Fig. 19 in Perna et al. 2020). For completeness, in Fig. B.1 we report the PV plots extracted along a PA$^{kin} \sim 40°$, with respect to the position of the two nuclei.

I16090 shows broadly regular gradient in V_* and V_{gas}, and a peak in σ_* at the position of the nucleus, as expected for rotation-dominated kinematics; on the other hand, $\sigma_{gas} \approx 130$ km/s along the entire extension of the major axis indicates highly perturbed gas kinematics.

I17208 shows broadly regular velocity profiles in both stellar and gas components; the velocity dispersion profiles are instead more irregular, with higher values toward the south-east direction, probably due to streaming motions (see also Fig. C.6).

I19297 No evidence of disk-like motions are present in the vicinity of the two nuclei of this system. The very high gas velocity dispersion (> 100 km/s) suggests the presence of strongly disturbed kinematics.

I19542 shows a clear gradient in V_* and a peak in σ_* at the position of the nucleus, as expected for rotation-dominated kinematics. On the other hand, the narrow Hα velocity profiles is irregular, mostly associated with blueshifted emission, and the $\sigma_{H\alpha} \approx 110$ km/s along the entire extension of the major axis indicates highly perturbed gas kinematics.

I20087 shows a clear gradient in V_* and a peak in σ_* at the position of the nucleus, as expected for rotation-dominated kinematics. The gas velocities broadly resemble the V_* profile, but reaching maximum velocities at ~ 2 kpc from the nuclear position a factor of ~ 2.6 higher than V_*. This behaviour might be
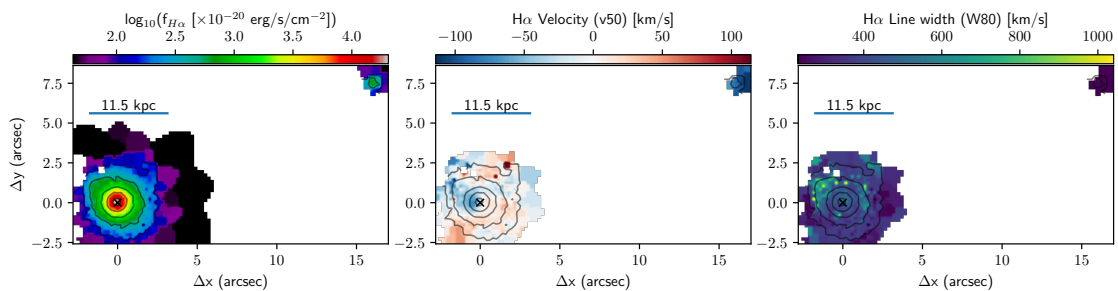
Fig. A.1: I00188 maps: Hα integrated flux (left), Hα centroid (*v*50, centre) and line-width (*W*80, right) obtained from the multi-component Gaussian fit. The first solid contour is 3σ and the jump is 0.5 dex. The cross marks the nucleus. North is up and West is right.
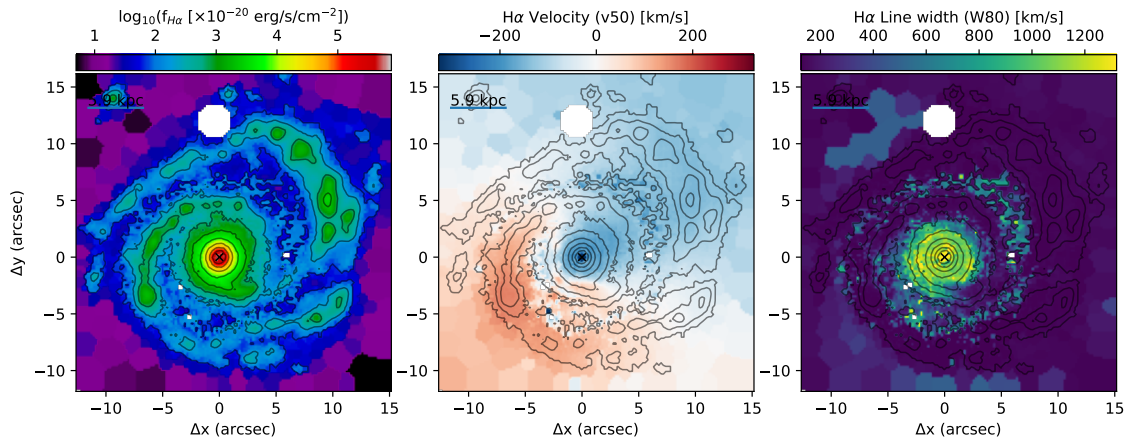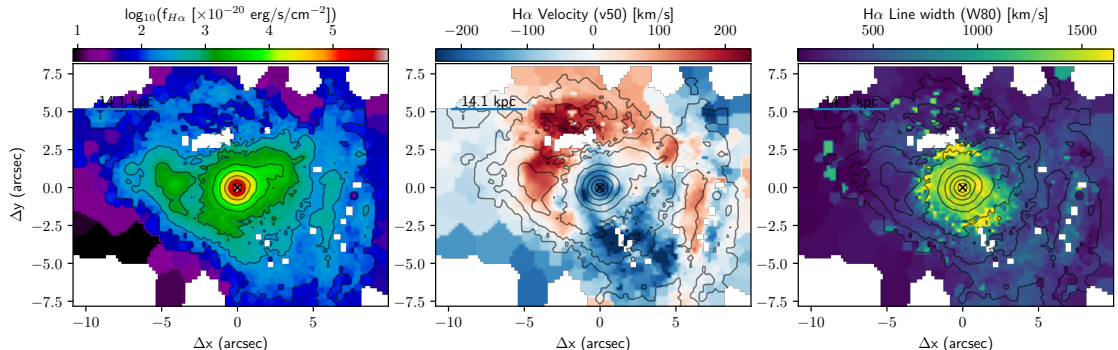

Fig. A.2: IZw1 maps. See Fig. A.1 for details.

Fig. A.3: I01572 maps. See Fig. A.1 for details.

due to the presence of a bi-conical outflow, and will be better investigated in a forthcoming paper.

20100 SE shows broadly regular velocity profiles in both stellar and gas components. We however observe a significant misalignment between the gas and stellar major axis PAs.

Appendix C: 3D-Barolo analysis

As already reported in Sect. 3.5, we followed two different methods to derive 3D-Barolo best-fit results. With the first method, we first tried to constrain the disk inclination using different azimuthal models spanning the almost entire range of inclinations ($i \in 5 - 85°$), selecting the i value with minimal residual. Fi-

nally, we ran 3D-Barolo with local models, fitting the rotation velocity v_{rot}, the velocity dispersion σ, and the major axis PA ϕ, using the disk inclination derived in the first step as initial guess. With the second method, we directly fit all disk kinematic parameters with a local model, by initialising the inclination to the value derived from the *Isophote* modelling of HST data (Sect. 2.2.2). The general fitting procedure is here explained in more details for each target in our sub-sample of PUMA systems with evidence of rotation.

IZw1: In this target, a correct ionised gas kinematic decomposition between disk and outflow components in the innermost nuclear regions is challenging. The strong outflow, the BLR and iron emission close to the Hα are responsible of a strong degen-
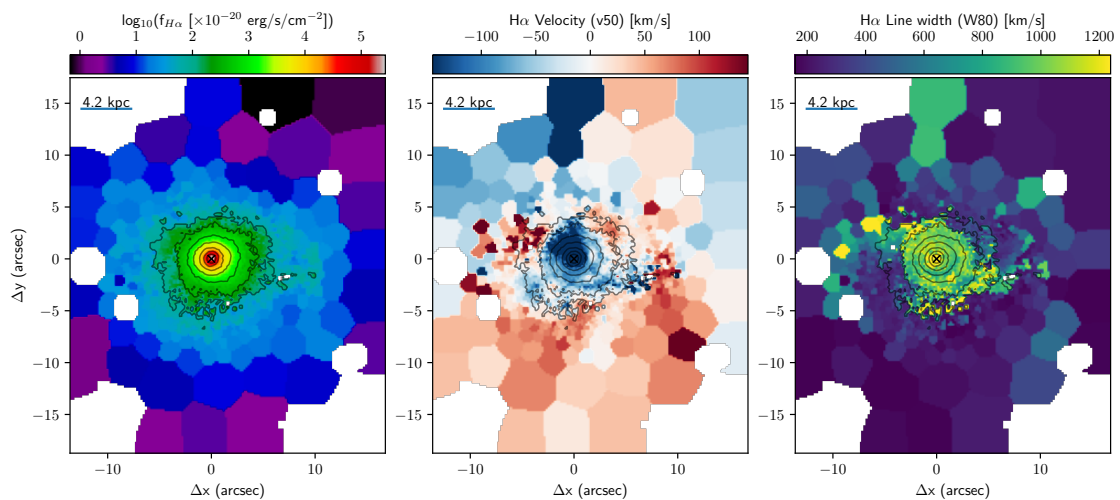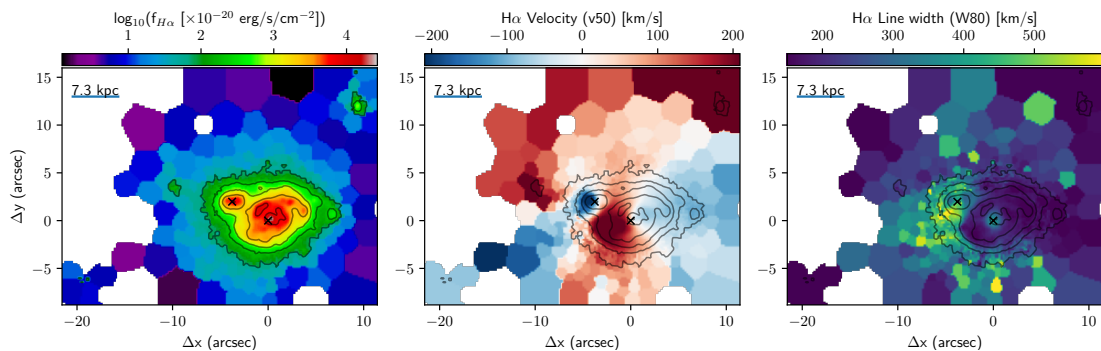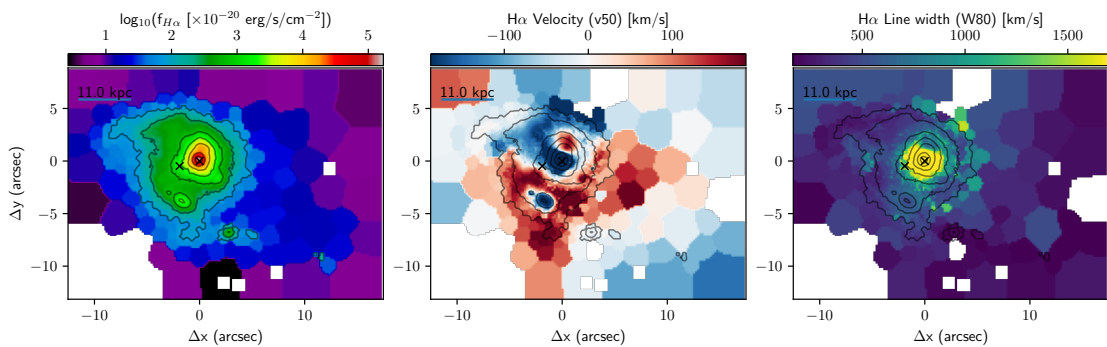
Fig. A.4: I0589 maps. See Fig. A.1 for details.
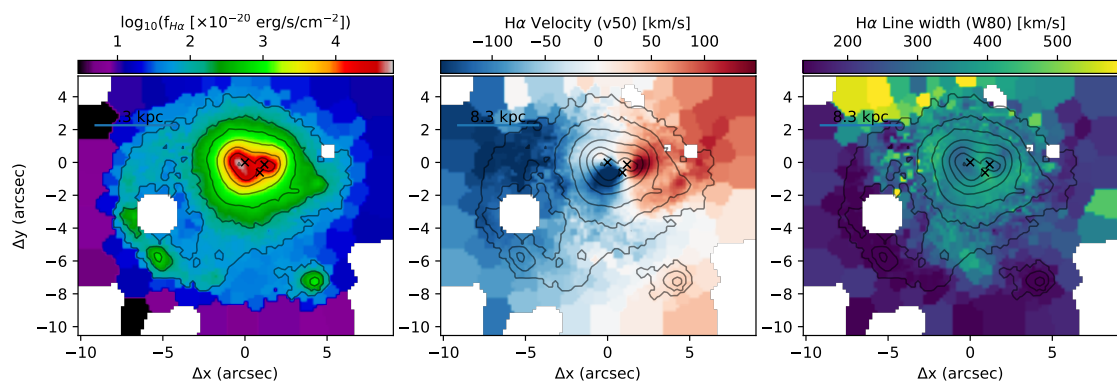
Fig. A.5: I07251 maps. See Fig. A.1 for details.
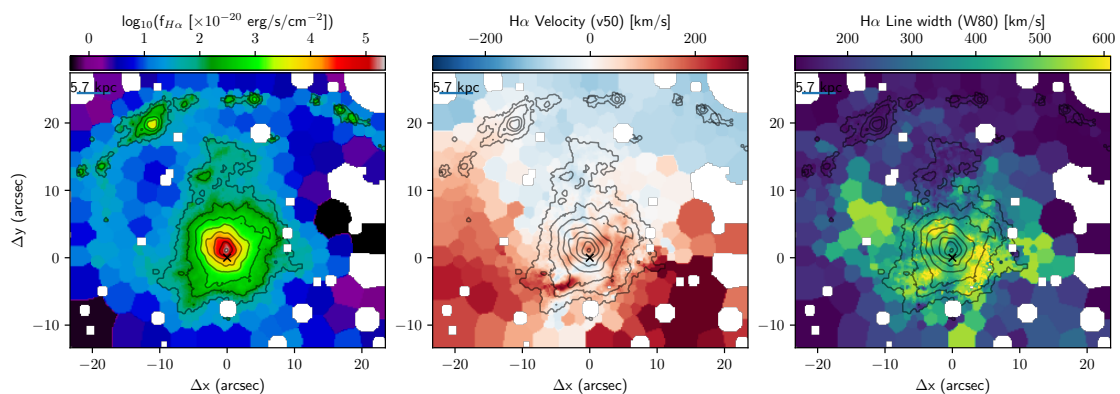
Fig. A.6: I09022 maps. See Fig. A.1 for details.

eracy in the multi-component Gaussian fit results. As a consequence, the narrow Hα map shown in the top-left panel of Fig. C.1 display a blueshifted kinematic component in the innermost nuclear regions not associated with disk kinematics. Similarly, the more extreme redshifted velocities in the south-east direction at ~ 3″ are reasonably due to the same fit degeneracy (see also Fig. A.2). On the contrary, the stellar kinematics (top-right panel in Fig. C.1) are more regular and display a clear rotation pattern.

The results obtained with I and II methods are broadly consistent (see Table 2), and point to an intermediate inclination of ~ 40° and a PA^{kin} ~ 140°, both consistent with the results presented in Tan et al. (2019) and derived from ALMA observations of the CO(1-0) molecular gas emission. 3D-Barolo fit results are reported in Fig. C.1. Significant residuals are observed in the innermost nuclear regions, due to the AGN driven outflow, and close to the spiral arms, probably due to the fact that 3D-Barolo

Fig. A.7: I10190 maps. See Fig. A.1 for details.
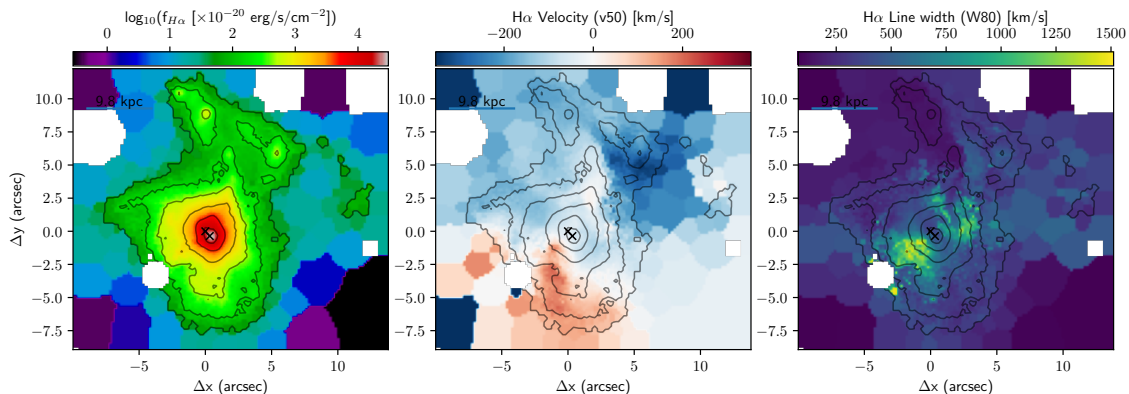
Fig. A.8: I11095 maps. See Fig. A.1 for details.
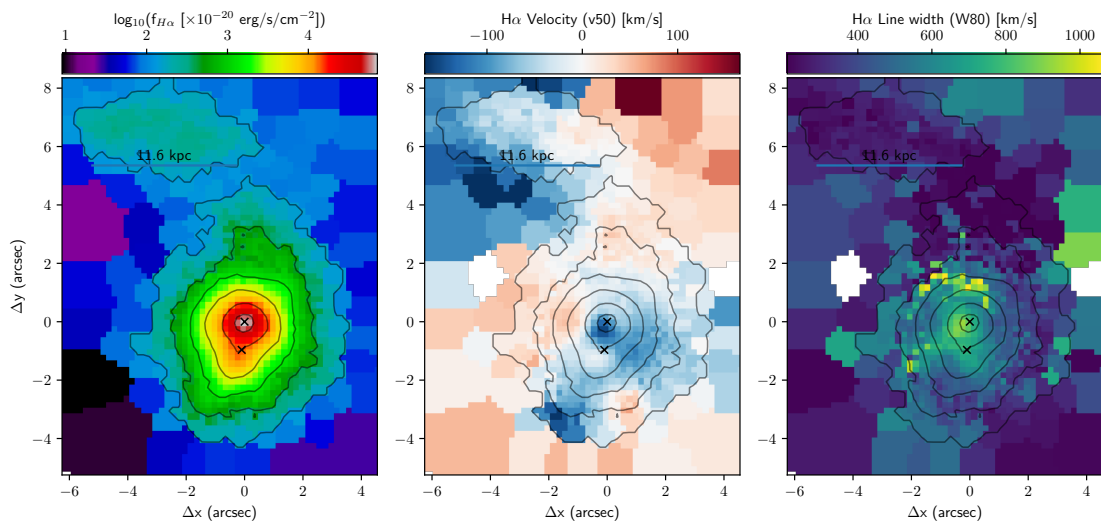
Fig. A.9: I12072 maps. See Fig. A.1 for details.

uses a concentric rings structure instead of spiral models to reproduce the observed kinematics.

I07251: This target shows two interacting nuclei at a projected distance of ~ 1.8 kpc, and very extended tails and streaming gas with velocities from ~ -150 km s^{-1}(north-east) to $\sim +150$ km s^{-1}(north-west). In the innermost nuclear regions, it presents disk-like motions, but with a kinematic centre not coincident with none of its two nuclei (Fig. A.5). I07251 flux dis-

tribution is very irregular, and cannot be modelled with elliptical isophotes.

We fitted the narrow Hα data cube with 3D-Barolo, following the I method strategy, fitting v_{rot}, σ, ϕ, and the kinematic centre position. Unfortunately, the data quality does not allow us to constrain the disk inclination in this target; we therefore performed the second step of the 3D-Barolo fit assuming a mean inclination of 52° (Bellocchi et al. 2013) as initial guess. The 3D-Barolo best-fit results are shown in Fig. C.2. Also for this
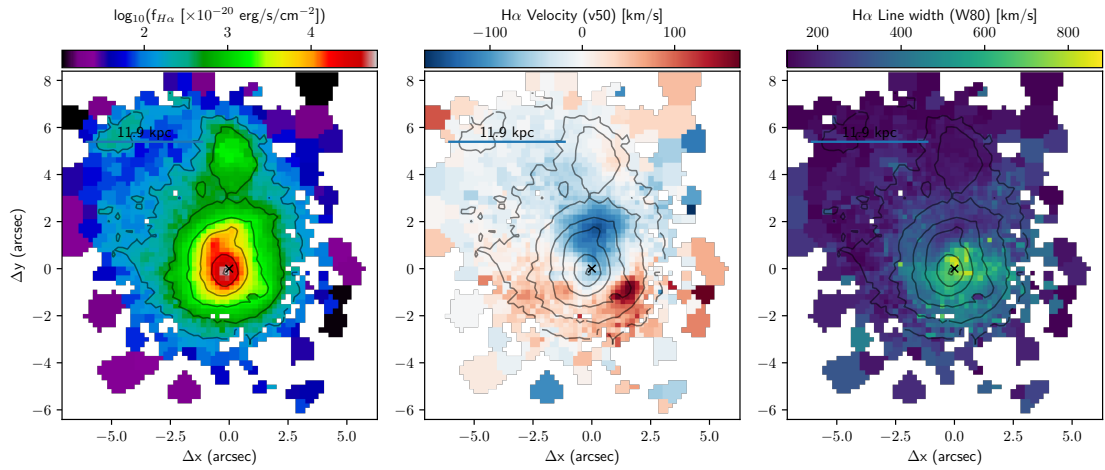
Fig. A.10: I13451 maps. See Fig. A.1 for details.
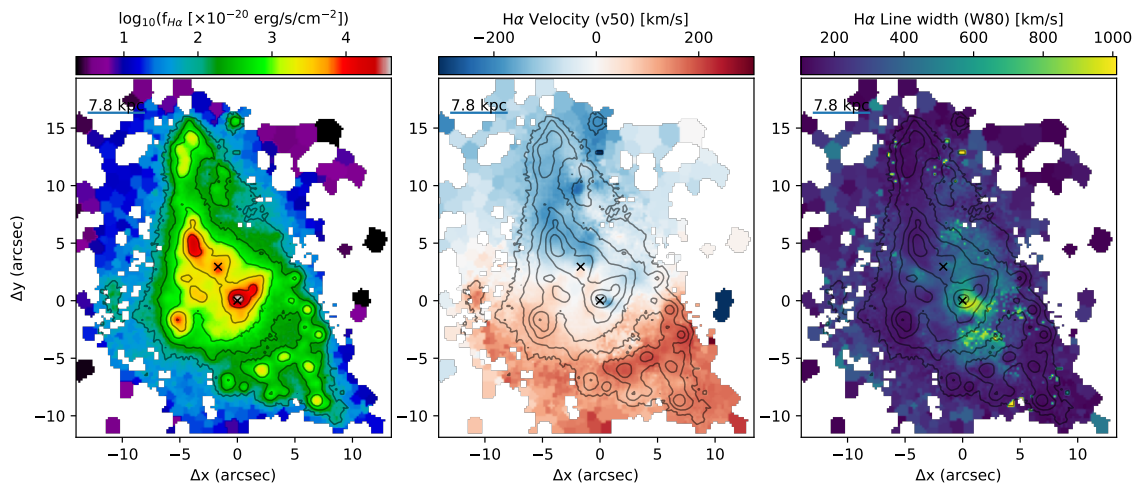
Fig. A.11: I14348 maps. See Fig. A.1 for details.
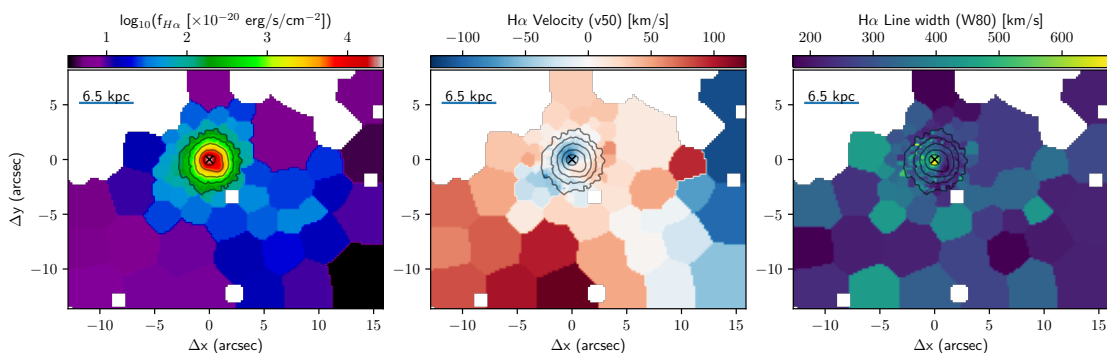
Fig. A.12: I14378 maps. See Fig. A.1 for details.

target, we observe significant residuals in the velocity and velocity dispersion maps, due to the complex nature of this interacting system.

I10190 W: I10190 shows two interacting nuclei at a projected distance of 7.2 kpc, and very extended tails and streaming gas with velocities from ~ -200 km s^{-1} (south-east) to $\sim +300$ km s^{-1} (north-west). Each nucleus shows disk-like kinematics on kpc scales (Fig. A.7); however, both the stellar and gas kinematics in the vicinity of the E nucleus are strongly affected by the presence of the W system motions (see e.g. Fig. B). This limits the possibility to study the E nucleus kinematics.

We fitted the I10190 W gas kinematics with both I and II methods, obtaining totally consistent results (Fig. C.3). Also for this target, we found a slightly offset between the near-IR nucleus and the fitted kinematic centre ($\sim 0.3''$); significant residuals are also observed in the 3D-Barolo maps.

I12072 N This source presents two nuclei, at a projected distance of 2.3 kpc, and a very extended plume in the north-east (Fig. A.9). Disk-like motions are presumably associated with the N nucleus. The flux distribution is complex, and does not allow us to perform a robust *Isophote* modelling. We therefore fitted the narrow Hα data cube with the 3D-Barolo, applying the
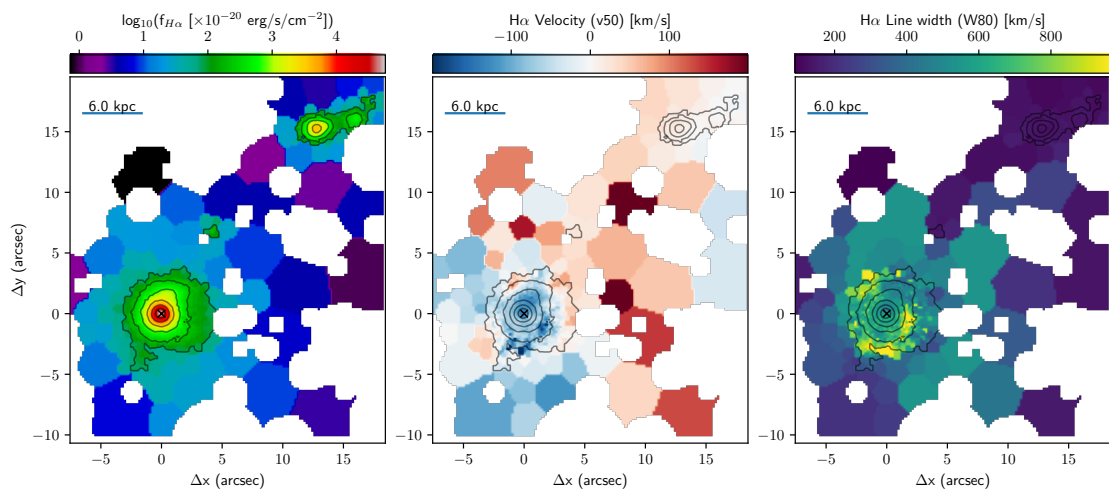
Fig. A.13: I16090 maps. See Fig. A.1 for details.
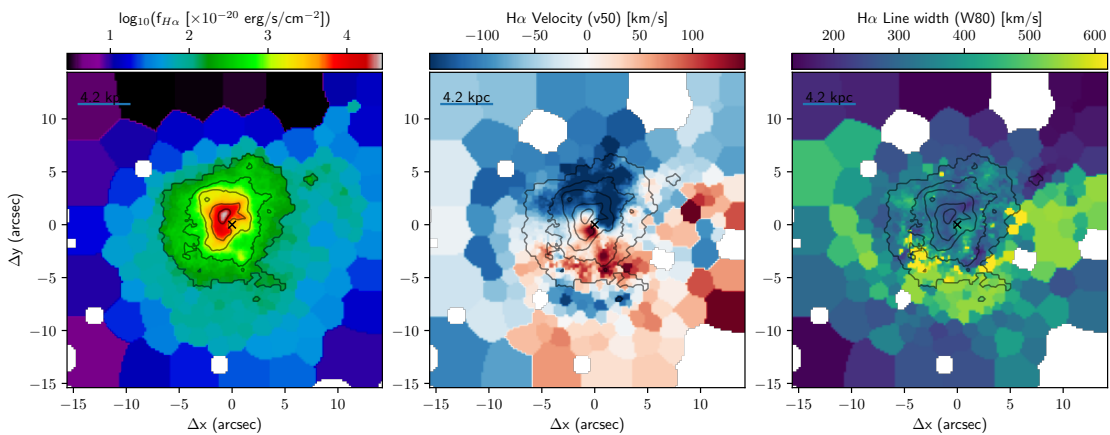
Fig. A.14: I17208 maps. See Fig. A.1 for details.
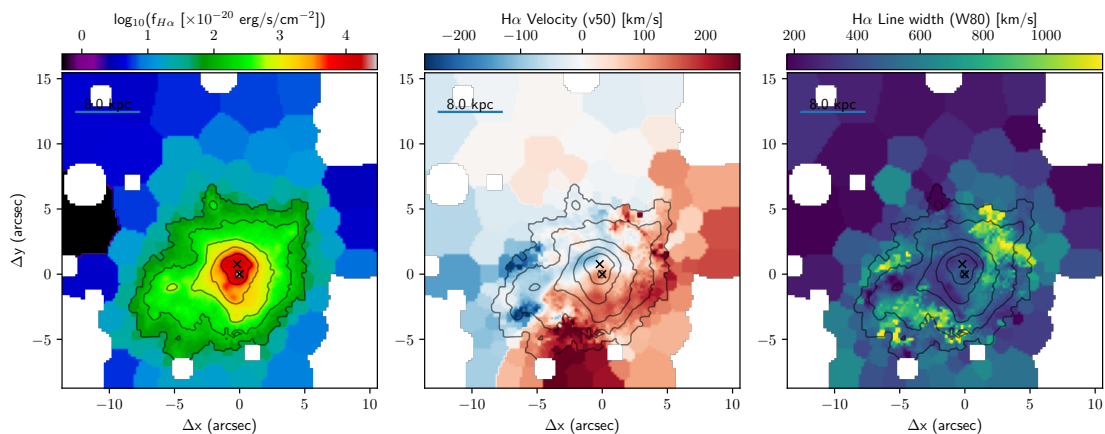
Fig. A.15: I19297 maps. See Fig. A.1 for details.

I method. The fit results are reported in Fig. C.4. Also in this case, velocity and velocity dispersion maps present significant residuals, due to the complex nature of this ULIRG.

I13120 The 3D-Barolo analysis is extensively presented in Sect. 3.5.

I14348 NE I14348 is an interacting ULIRG with two nuclei at a projected distance of 5.3 kpc. The NE nucleus presents disk-like motions, while the SW kinematics are dominated by a strong outflow pointing to south-west; streaming motions along the north-east south-west direction are also present on scales of 10s kpc (Fig. A.11). We fitted with 3D-Barolo the kinematics

Fig. A.16: I19542 maps. See Fig. A.1 for details.
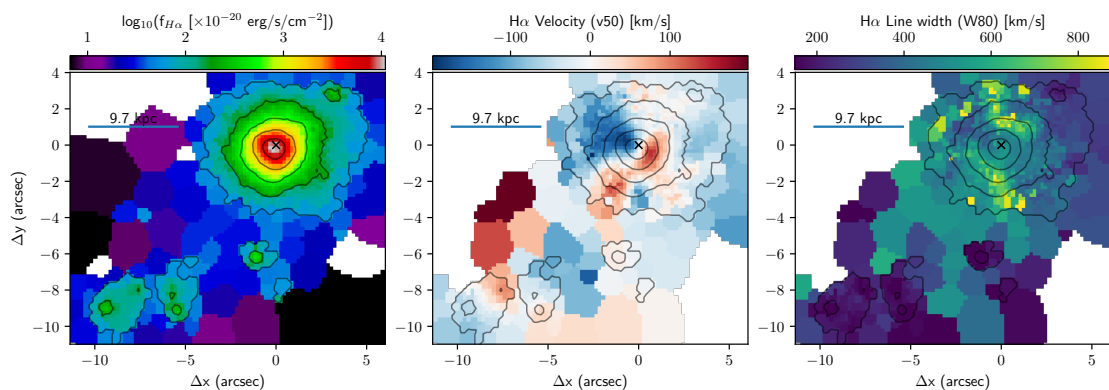
Fig. A.17: I20087 maps. See Fig. A.1 for details.
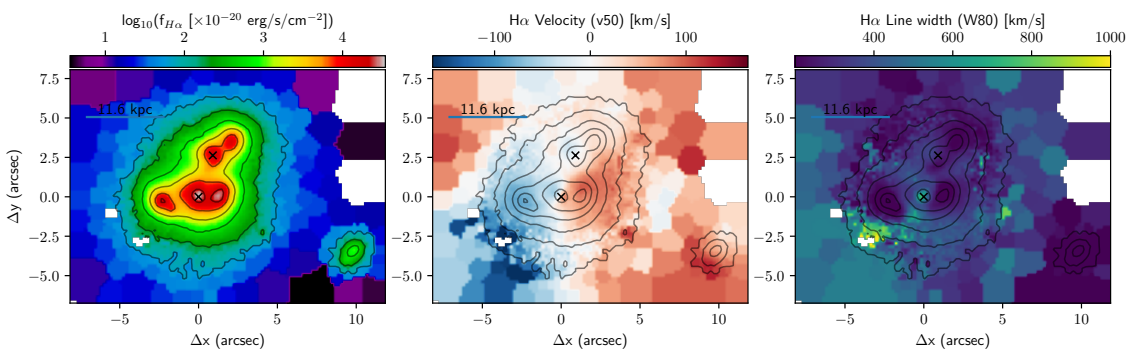
Fig. A.18: I20100 maps. See Fig. A.1 for details.

in the NE nuclear region, applying the I method to infer, as a first step, the inclination of the disk. In fact, the complex nature of this interacting system prevents robust *Isophote* analysis and no morphological information is available. We decided to limit the 3D-Barolo fit analysis to the innermost nuclear regions ($\sim 3'' \times 3''$), in order to exclude the contribution from the large scale streaming motions. As a consequence, the disk inclination we determined with the I method, $52° \pm 3°$, has to be taken with caution. The fit results are reported in Fig. C.5. Significant residuals are observed in the velocity and velocity dispersion maps.

The kinematic centre has been fixed at the position of the nucleus during the 3D-Barolo analysis, as no significant variations in fit results are observed considering the kinematic centre position as free parameter.

I17208 This source presents disk-like kinematics and extended tidal tails with velocities from ~ -150 km s^{-1}(north) to $\sim +150$ km s^{-1}(south-west; see Fig. A.14). For this target, we decided to exclude from the 3D-Barolo analysis the more external regions, associated with streaming motions; as a result, I method does not provide robust constraints for the disk inclination. We
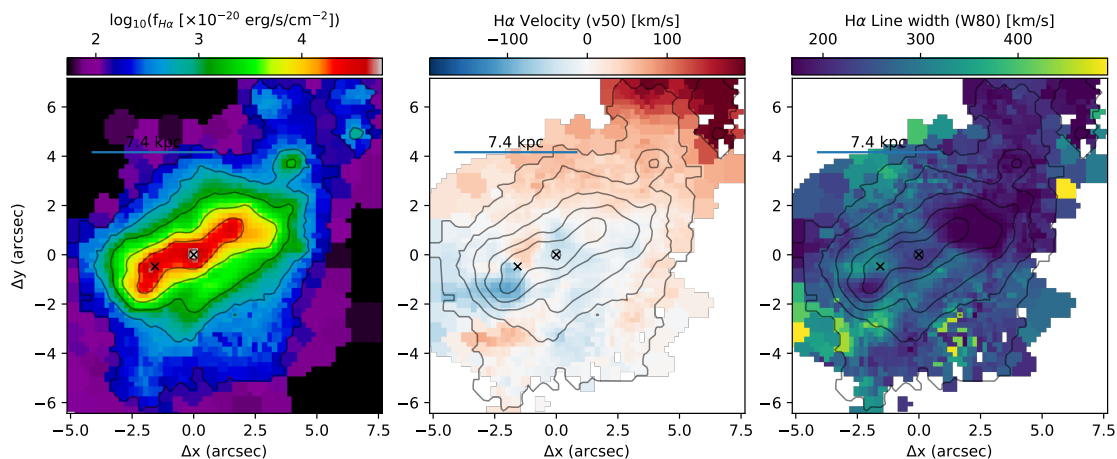
Fig. A.19: I22491 maps. See Fig. A.1 for details.

therefore applied the II method, assuming a disk inclination of 40° (from *Isophote* analysis) as initial guess. The 3D-Barolo fit results are reported in Fig. C.6. The kinematic centre has been fixed at the position of the nucleus during the 3D-Barolo analysis; no significant variations in fit results are obtained adding the kinematic centre position as free parameter.

I20100 SE The I20100 ULIRG is an interacting system with two nuclei at a projected distance of 6.5 kpc. The SE nucleus presents disk-like motions, while the NW kinematics are more complex and probably affected by the streaming motions (Fig. A.18). We therefore decided to analyse with 3D-Barolo the kinematics in the vicinity of the SE nucleus only.

The results obtained with methods I and II are broadly consistent (see Table 2), and point to an inclination of $\sim 58°$ and a $PA^{kin} \sim 287°$. The significant difference between gas and stellar PA^{kin} might suggest more complex kinematics in the innermost nuclear regions of this source; indeed, we observe significant residuals in the velocity and velocity dispersion maps (Fig. C.7) along the gas kinematic minor axis.

Appendix D: Extended sample of SB disk galaxies

In this section, we introduce the additional individual ionised gas measurements of SB disk galaxies reported in Fig. 7. In particular, we select:

- the $H\alpha$ (narrow component) velocity dispersion of 33 LIRGs and one ULIRG with disk kinematics from Bellocchi et al. (2013, B13 in the figure), observed with VLT/VIMOS, and the $Br\gamma$ velocity dispersion of 7 LIRGs from Crespo Gómez et al. (2021, C21 in the figure), observed with VLT/SINFONI. All these systems are characterised by mean σ of the order of several 10s km s^{-1};

- the $H\alpha$ velocity dispersion of 22 rotationally supported dusty galaxies of the cluster Cl0024+17 at $z \sim 0.4$ (Johnson et al. 2016, J16 in the figure), observed with VLT/FLAMES. These systems, with their median $v_{rot}/\sigma = 5 \pm 2$ and their SFRs likely enhanced by the effects of ram pressure, also tend toward higher values compared to MS galaxies at the same redshift;

- the $H\alpha$ velocity dispersion of eight (U)LIRGs at $z \sim 0.2 - 0.4$ from Pereira-Santaella et al. (2019, PS19 in the figure), observed with the optical integral field spectrograph SWIFT.

Most of them are interacting systems (6/8), and have relatively small v_{rot}/σ ratios (from 0.4 to 3.2);

- the $Pa\alpha$ velocity dispersion of three SB disk galaxies at $z \sim 0.15$ presented in Molina et al. (2020, M20 in the figure), and observed with SINFONI;

- the $H\alpha$ velocity dispersion of seven disk galaxies at $z \sim 2$ from the SINS/zC-SINF AO Survey, presented in Förster Schreiber et al. (2018, FS18 in the figure): ZC400528, ZC406690, ZC407302, ZC410123, ZC411737, ZC413507, and ZC415876. These galaxies display an offsets by a factor of $\gtrsim 4$ in SFR from the MS in their Fig. 6, and $\sigma_0 \sim 30 - 60$ km s^{-1};

- the $H\alpha$ velocity dispersion of a starburst disk galaxy at $z = 2.028$, SMM J0217-0503b, merging with an AGN source (at a projected distance of ~ 15 kpc), from Alaghband-Zadeh et al. (2012, A12 in the figure), and observed with VLT/SINFONI;

- the $H\alpha$ velocity dispersion of a SB disk galaxy at $z = 2.24$, SHiZELS-14, from Cochrane et al. (2021, Co21 in the figure). This source has been observed with the adaptive optics assisted VLT/SINFONI spectrograph;

- the [OIII] (narrow component) velocity dispersion of a submm bright disky galaxy hosting a broad line quasar, SMM J1237+6203 at $z = 2.075$, from Harrison et al. (2012), and observed with Gemini-North NIFS.

All these measurements have been obtained from IFS data. For the B13, C21, J16, A12 and H12 sources, σ_0 was computed as a mean velocity dispersion across the galaxy extension in the FOV; PS19 σ_0 were inferred from GalPak^{3D} modelization (correcting for the beam-smearing and line-spread-function broadening), which assumes a spatially constant velocity dispersion in the disk; FS18 σ_0 were measured along the kinematic major axis at the largest radii possible, away from the central peak caused by the steep inner disk velocity gradient; M20 and Co21 σ_0 were instead derived as mean velocity dispersion in the external regions of the sources, excluding the innermost regions affected by beam smearing.
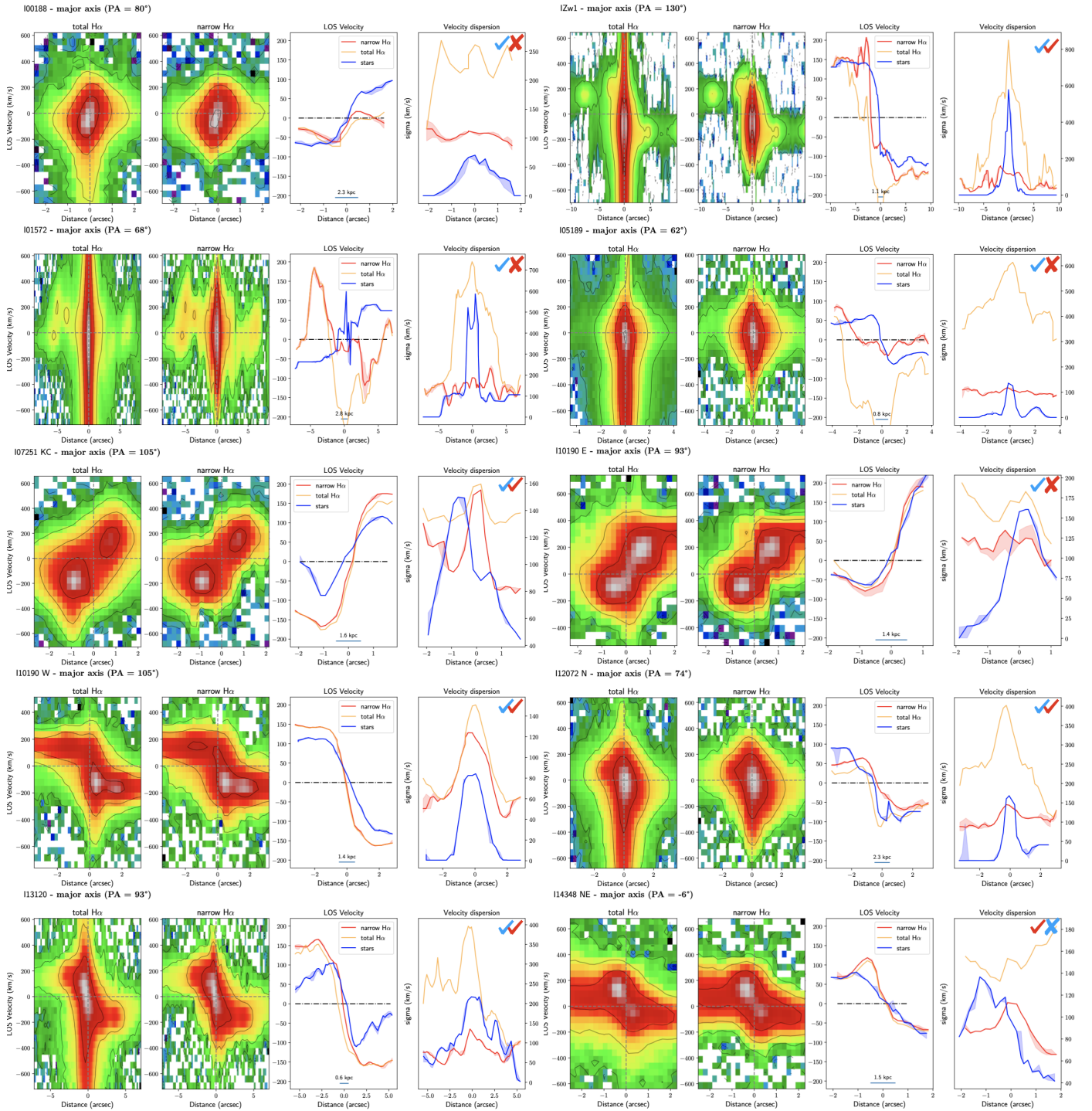
Fig. B.1: Position-velocity diagrams along the galaxy major axis for all PUMA systems showing i) a well defined velocity gradient along the major axis, and ii) a peak in the velocity dispersion diagram close to the position of the nucleus. These two conditions provide initial evidence for rotation-dominated kinematics. All systems which gas (stellar) kinematics satisfy the two conditions are marked with a blue (red) check-mark in the top-right corner of the velocity dispersion panel; on the contrary, the systems not satisfying at least one of the two conditions are marked with a cross symbol; more uncertain kinematics are marked with a question mark. The system for which the gas *and* the stellar components are not satisfying the two conditions are not reported in figure. Line velocity centroids and line widths of narrow Hα, total Hα and stars are reported for each target, as labeled. See Fig. 4 for further details about the individual panels.
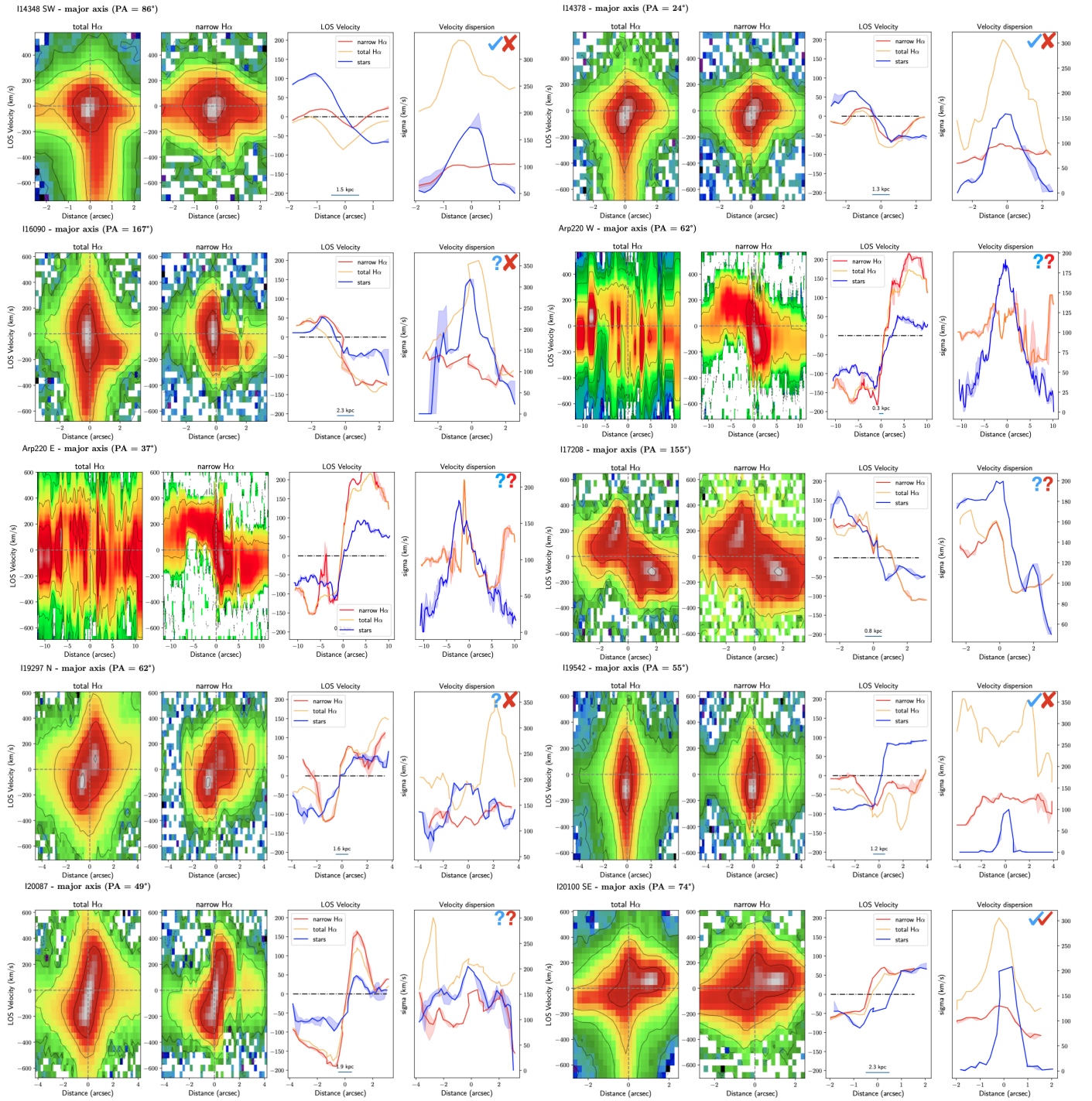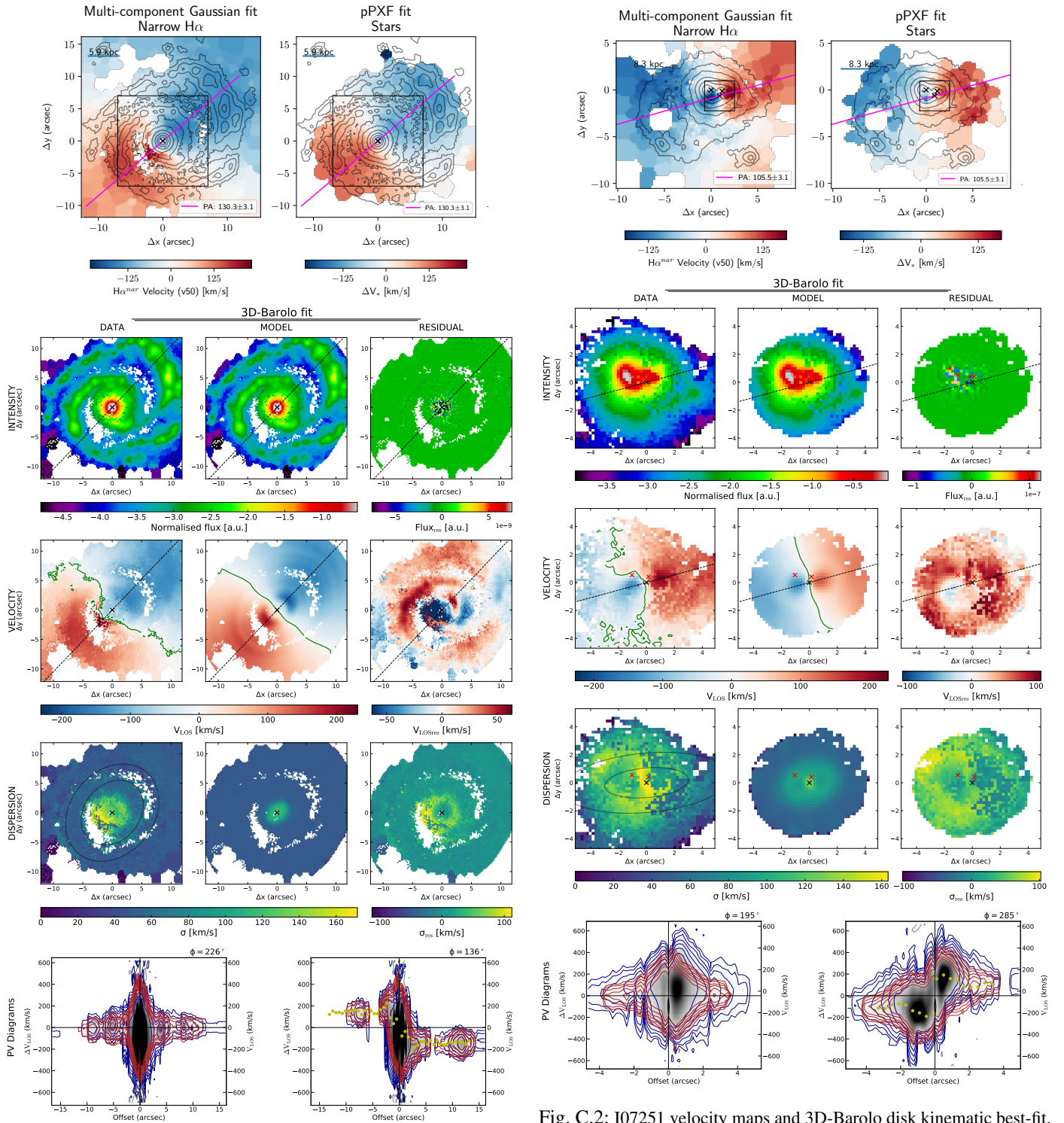
Fig. B.1: Continued.

Fig. C.1: IZw1 velocity maps and 3D-Barolo disk kinematic best-fit. *Top panels*: narrow Hα (left) and pPXF stellar (right) velocity maps. The magenta line identifies the major axis PA measurement, computed within the black box region; the black cross identifies the nucleus. *Second-to-fourth row panels*: comparison of 3D-barolo data and model moment maps, as labeled in the figure. In the intensity and velocity maps, we reported the major axis PA (dashed line), and the position of the kinematic centre (black cross); the green curve in the velocity maps represent the zero-velocity axis. In the dispersion map on the left, the black curves show the region from which the median σ_0 value has been derived. *Bottom panels*: PV diagram along the major axis (right) and minor axis (left) for both data (grey map and blue contours) and best-fit model (red contours, and yellow dots associated to individual concentric rings used to model the data).

Fig. C.2: I07251 velocity maps and 3D-Barolo disk kinematic best-fit. In this target, the kinematic centre is shown with a black cross, while the two ULIRG nuclei with red crosses. See Fig. C.1 for further details.
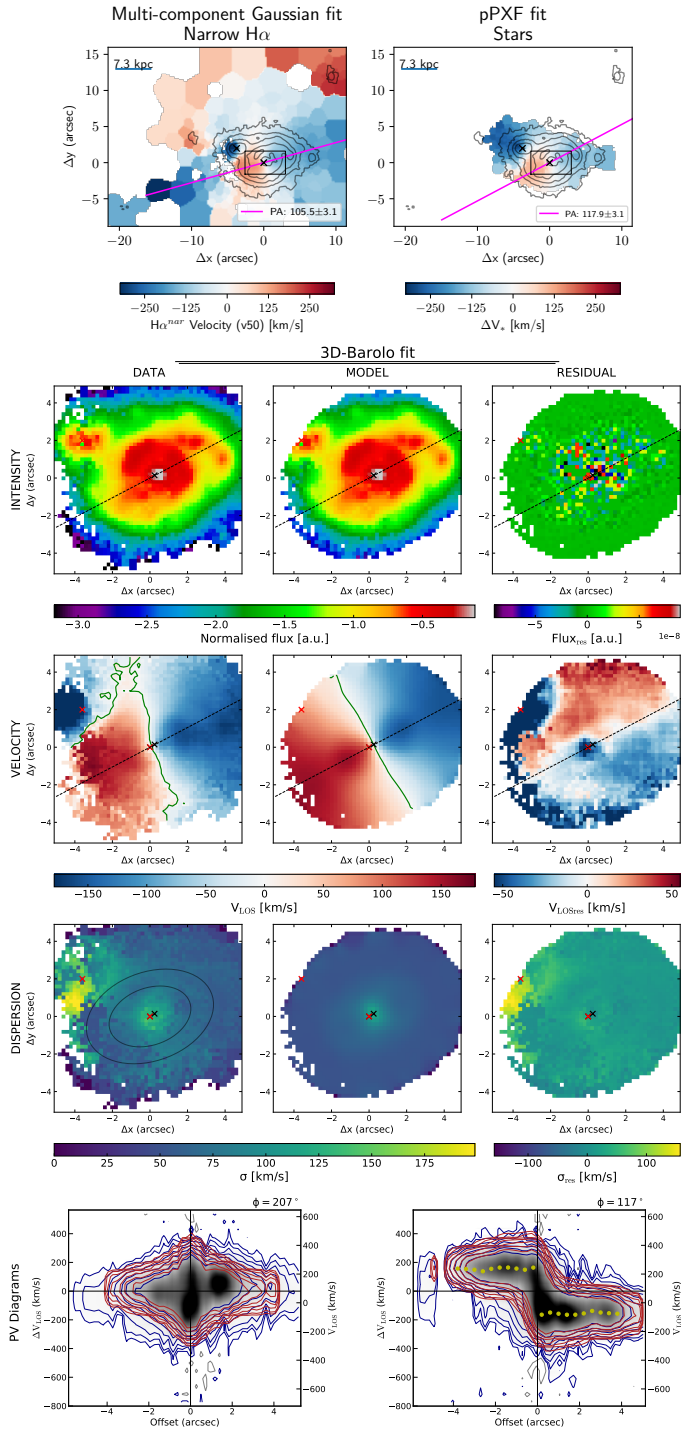
Fig. C.3: I10190 W velocity maps and 3D-Barolo disk kinematic best-fit. See Fig. C.1 for further details.
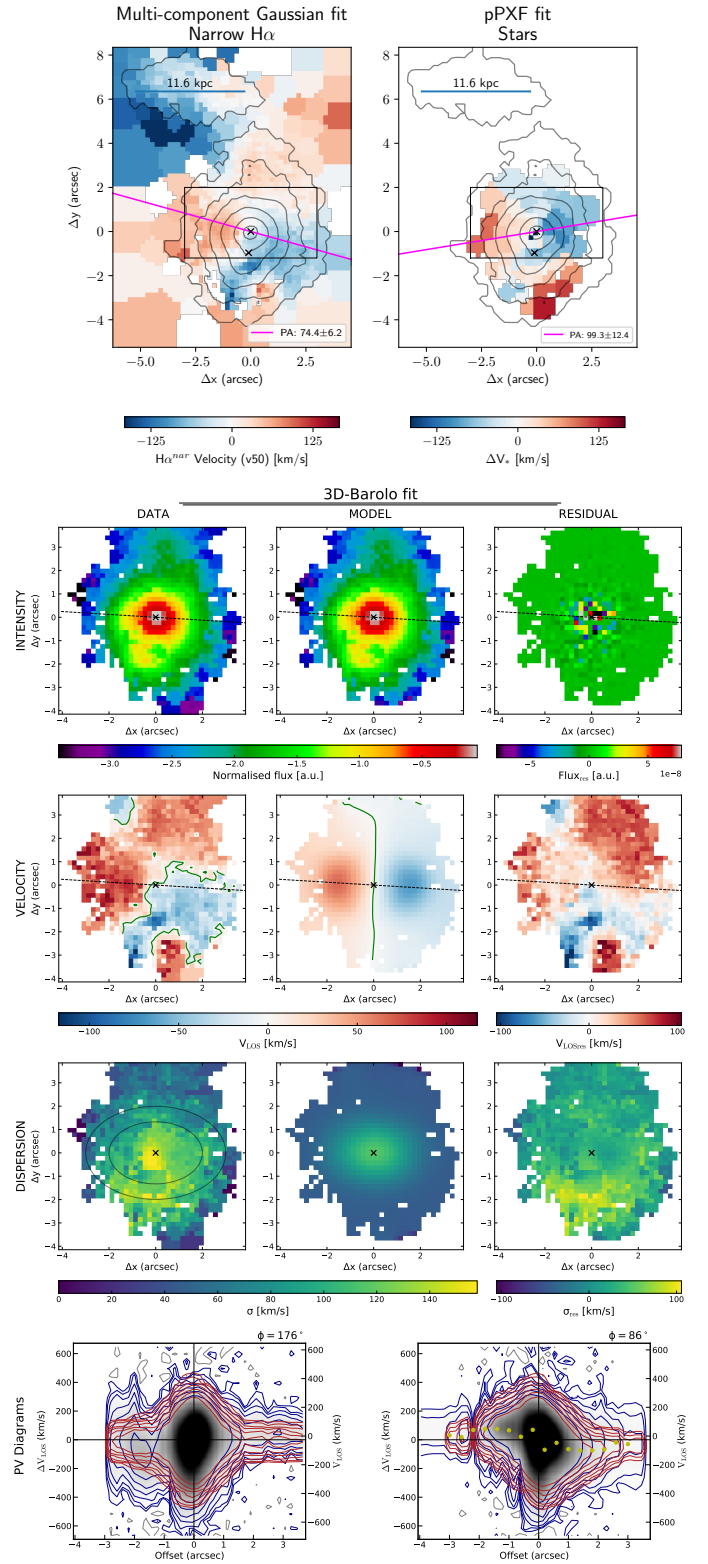
Fig. C.4: I12072 velocity maps and 3D-Barolo disk kinematic best-fit. See Fig. C.1 for further details.
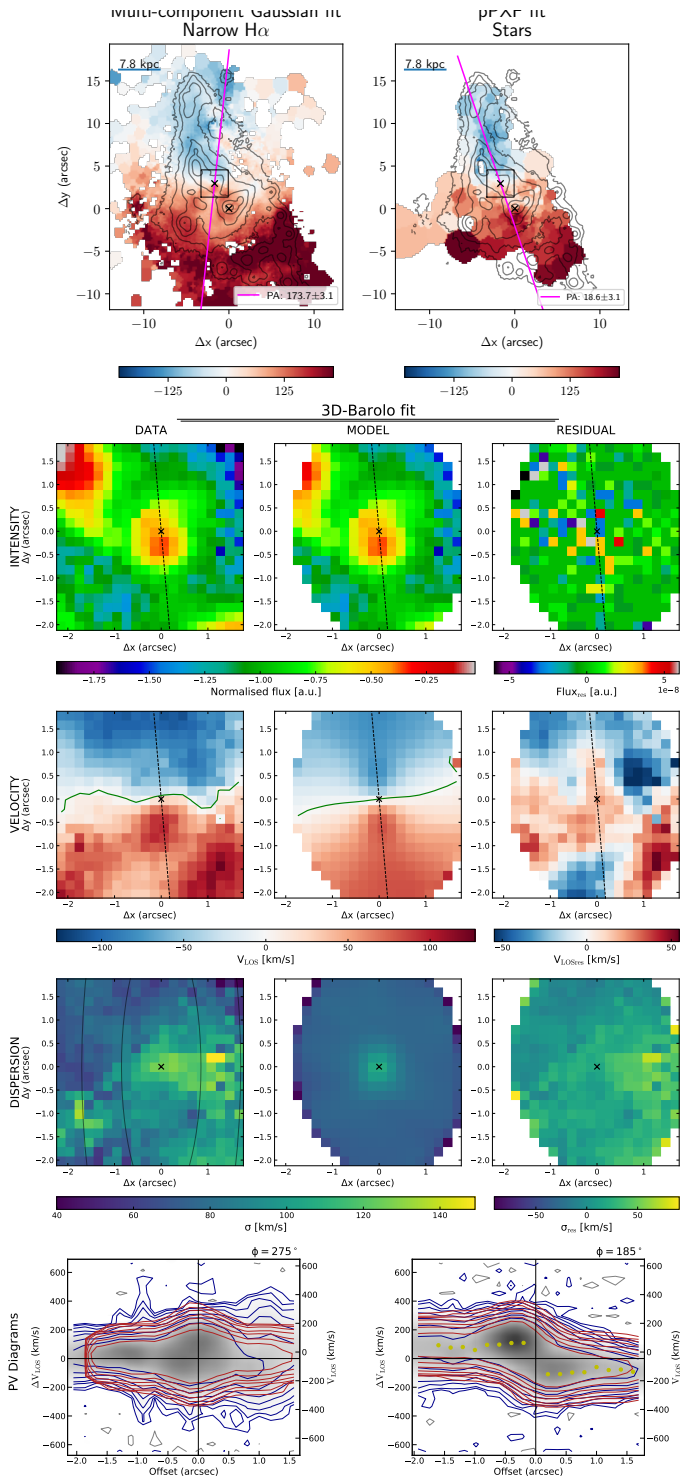
Fig. C.5: I14348 NE velocity maps and 3D-Barolo disk kinematic best-fit. See Fig. C.1 for further details.
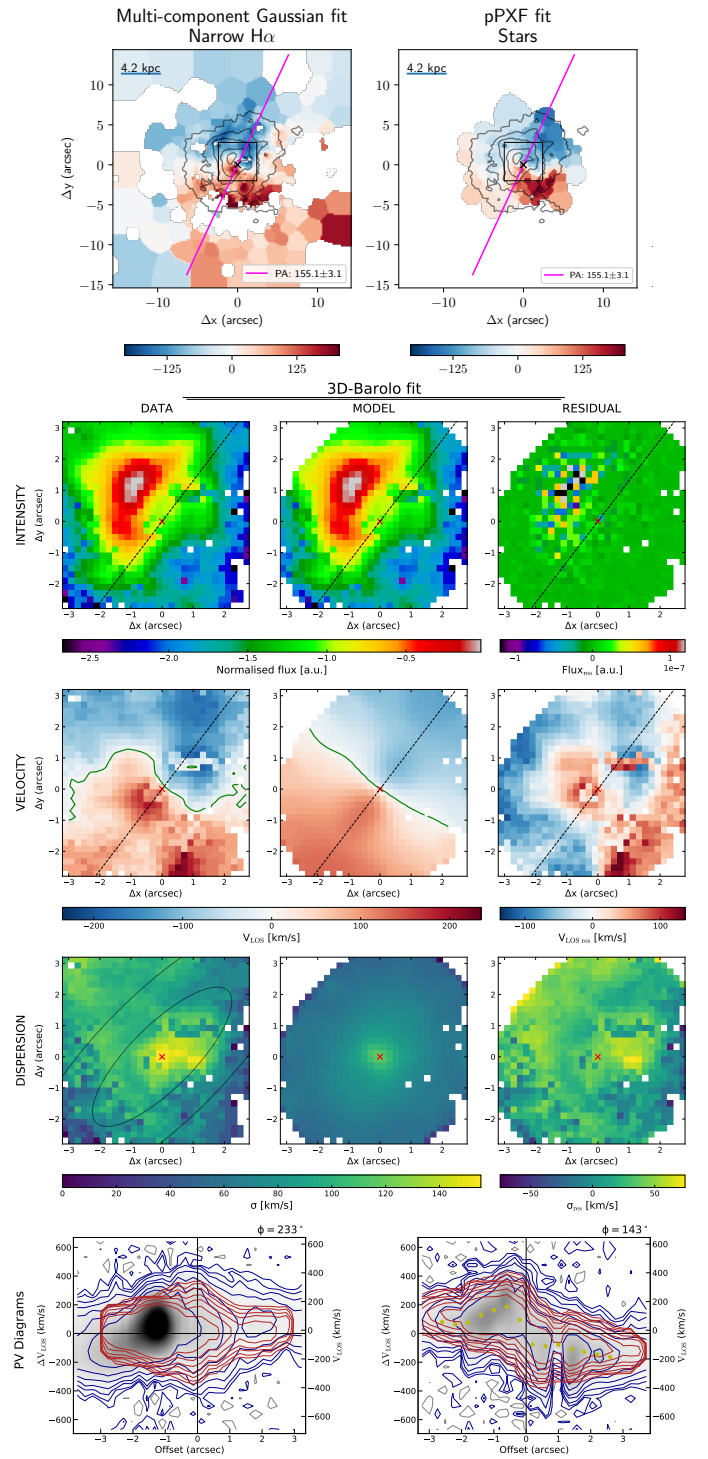
Fig. C.6: I17208 velocity maps and 3D-Barolo disk kinematic best-fit. See Fig. C.1 for details.
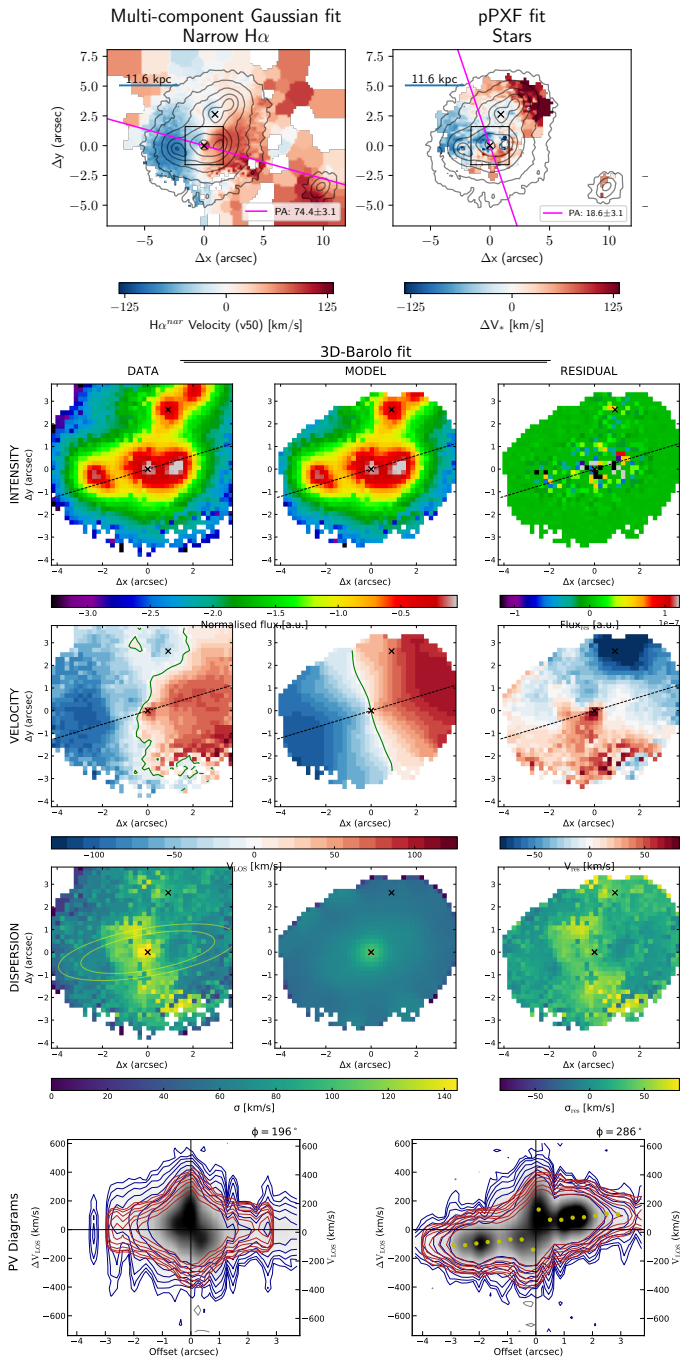
Fig. C.7: I20100 SE velocity maps and 3D-Barolo disk kinematic best-fit. See Fig. C.1 for details.